

Kinematic Rupture Generator Based on 3-D Spontaneous Rupture Simulations Along Geometrically Rough Faults

 W. H. Savran¹  and K. B. Olsen² 
¹Southern California Earthquake Center (SCEC), University of Southern California, CA, Los Angeles, USA, ²Department of Geological Sciences, San Diego State University, CA, USA
Key Points:

- Our proposed rupture generator is based on statistics from 100 + dynamic simulations on geometrically complex faults
- Dynamic rupture models follow scaling relationships for $M_{6.4-7.2}$ strike-slip events and provide source spectra comparable with observations
- Ground motions from kinematic model reproduce leading ground motion prediction equations and produce flat acceleration spectra up to 10 Hz

Supporting Information:

- Supporting Information S1
- Figure S1
- Figure S2

Correspondence to:
 W. H. Savran,
wsavran@gmail.com
Citation:

Savran, W. H., & Olsen, K. B. (2020). Kinematic rupture generator based on 3-D spontaneous rupture simulations along geometrically rough faults. *Journal of Geophysical Research: Solid Earth*, 125, e2020JB019464. <https://doi.org/10.1029/2020JB019464>

Received 24 JAN 2020

Accepted 2 SEP 2020

Accepted article online 9 SEP 2020

Abstract Spontaneous rupture simulations along geometrically rough faults have been shown to produce realistic far-field spectra and comparable fits with ground motion metrics such as spectral accelerations and peak motions from Ground Motion Prediction Equations (GMPEs), but they are too computationally demanding for use with physics-based probabilistic seismic hazard analysis efforts. Here, we present our implementation of a kinematic rupture generator that matches the characteristics of, at least in a statistical sense, rough-fault spontaneous rupture models. To this end, we analyze ~100 dynamic rupture simulations on strike-slip faults with M_{w} ranging from 6.4 to 7.2. We find that our dynamic simulations follow empirical scaling relationships for strike-slip events and provide source spectra comparable to a source model with ω^{-2} decay. To define our kinematic source model, we use a regularized Yoffe function parameterized in terms of slip, peak-time, rise-time, and rupture initiation time. These parameters are defined through empirical relationships with random fields whose one- and two-point statistics are derived from the dynamic rupture simulations. Our rupture generator reproduces Next Generation Attenuation (NGA) West2 GMPE medians and intraevent standard deviations of spectral accelerations with periods as short as 0.2 s for ensembles of ground motion simulations. Our rupture generator produces kinematic source models for $M_{6.4-7.2}$ strike-slip scenarios that can be used in broadband physics-based probabilistic seismic hazard efforts or to supplement data in areas of limited observations for the development of future GMPEs.

1. Introduction

Most buildings have resonance frequencies between 1 and 10 Hz, with single-family houses in the upper part of that range. Therefore, it is important to understand the behavior of these high-frequency waves to predict shaking from future earthquakes. Broadband physics-based ground motion simulations can provide insight into ground motions from future earthquakes; however, computing the high-frequency wave field poses significant challenges. In addition to understanding the small-scale properties of the Earth's crust and upper mantle, accurately characterizing the high-frequency behavior (>1 Hz) of the earthquake's source still remains a largely unsolved problem.

One promising approach to generate realistic broadband ground motion simulations uses dynamic rupture calculations along geometrically rough faults. Geologists have observed that faults include roughness over several decades of scale lengths (Candela et al., 2012). Fault roughness introduces heterogeneous shear and normal tractions that result in complex rupture behavior. Dunham et al. (2011) and Shi and Day (2013) have shown that more complexity in the rupture process decreases the coherency of the wave front, typically reducing the peak amplitudes and increasing the duration of the resulting ground motions. In summary, these studies show that dynamic rupture simulations along rough faults can produce characteristics of observed ground motions such as flat acceleration spectra over a broad range of frequencies.

While dynamic rough-fault models have been shown to capture a number of key features of recorded ground motions, its modeling advantages come at a high computational cost. In contrast with dynamically computed source models, kinematic earthquake sources provide a priori descriptions of the spatiotemporal evolution of slip along a fault interface. Kinematic earthquake sources can be constructed using information resulting from finite-fault inversions (e.g., Mai & Beroza, 2002), dynamic rupture simulations (e.g., Graves & Pitarka, 2016; Schmedes et al., 2010, 2013; Song, 2015; Song et al., 2013; Trugman & Dunham, 2014), or theoretical considerations regarding earthquake rupture (e.g., Andrews, 1980; Guatteri et al., 2004). Typically, a kinematic rupture model is generated using a stochastic distribution of slip and relating the

remaining rupture parameters through direct correlations or empirical relationships derived from various earthquake source studies. Most kinematic earthquake source models introduce heterogeneity into the rupture through stochastic spatial fields used to define the rupture process. These fields are used to parameterize a slip rate function that describes the temporal evolution of slip on each subfault. The choices of slip rate functions are by no means unique and differ based on the individual implementation of the kinematic rupture generator (KRG).

Currently, both deterministic and so-called hybrid ground motion simulations use KRGs (e.g., Graves & Pitarka, 2014; Olsen & Takedatsu, 2015) or directly incorporate the dynamic rupture description (e.g., Olsen et al., 2009; Roten et al., 2014; Withers et al., 2019,b) to define their input source models. Kinematic rupture generators provide a computational convenience, as large dynamic rupture simulations are too computationally expensive for physics-based probabilistic seismic hazard efforts such as the Southern California Earthquake Center (SCEC) CyberShake (Graves et al., 2011) or the SCEC Broadband Simulation Platform (Goulet et al., 2015) that require large ensembles of rupture realizations.

In this manuscript, we present our implementation of a KRG based on 3-D rough-fault dynamic rupture simulations. This manuscript is organized as follows: first, we provide an overview of the dynamic rupture simulations and the general framework used for our KRG. Next, we follow with an explanation of the statistical relationships derived from the dynamic rupture calculations used to generate our kinematic sources. Finally, we show examples of 0–10 Hz fully deterministic ground motions originating from these KRG sources and comparisons against NGA-West2 GMPEs in order to validate our rupture generator.

2. Dynamic Rupture Simulations

2.1. Modeling Overview

2.1.1. Dynamic Rupture Code

We used the Support Operator Rupture Dynamics (SORD) code to compute our dynamic rupture simulations. SORD is a second order in space and time finite-difference solution to the elastodynamic equation including a split-node fault boundary condition to allow for dynamic rupture (Ely et al., 2008, 2009). SORD uses a structured nonregular mesh and incorporates Drucker-Prager plasticity along with both rate-and-state friction and slip-weakening friction models (Shi & Day, 2013). In total, we computed 108 dynamic rupture simulations to analyze for constructing the KRG.

2.1.2. Fault Geometry, Mechanism, and Magnitude Range

We computed all ruptures on right-lateral strike-slip faults with mean vertical fault planes. The models in the database range in M_w between 6.4 and 7.2. The variability in our database results from differing rough fault geometries and choice of initial model parameters. We used the same mesh dimensions for all simulations, but the actual rupture length (and M_w) is determined a posteriori by the rupture process. We impose a maximum rupture length of 60 km and include a velocity-strengthening zone at the base of the fault limiting the effective fault width to 15–17 km. Each simulation uses $dx = 25$ m and has dimensions of 65 km \times 40 km \times 20 km with 20 node wide perfectly matched layers (Ely et al., 2008) in order to minimize artifacts in the rupture due to boundary reflections.

2.1.3. Friction and Stress Models

We include both strongly rate-weakening and slip-weakening friction models in our rupture database along with models incorporating plasticity. The frictional parameters are based on previously published studies by Shi and Day (2013) and the SCEC Rupture Validation exercises (Harris et al., 2009). All simulations share the same 1-D background velocity model with $\min(V_z) = 1,250$ m/s, which is derived from a model representing a typical hard-rock site in southern California. We assume two different models for the general behavior of the initial stress field. One model has linearly increasing normal-stress which is assumed to be lithostatic (i.e., $\tau_n = (\rho_b - \rho_w)gz$, where ρ_b is the bulk density given by the velocity model, ρ_w is the density of water assumed to be 1,000 kg/m³, and g represents acceleration due to gravity). The second model includes depth-dependent lithostatic normal stress to $z = 8$ km, and constant normal stress where $z > 8$ km; the water table is assumed to be at the surface. This formulation provides ruptures that have stress drop distributions consistent with observations of earthquakes in southern California (Shearer et al., 2006). A physical explanation for this model comes from an increase of pore pressure with depth, creating a constant effective normal stress. Our rupture models include different levels of prestress with

most models having $\tau_s \approx 0.3$. In all ruptures the maximum compressive stress is set to 45° relative to the mean fault plane.

In the slip-weakening ensembles, we define two different sets of frictional parameters, each resulting in the same average static stress drop of $\Delta\sigma = 5$ MPa. We use values of the initial friction μ_0 of 0.225 and 0.3 to be consistent with observations of the low magnitude of shear stress on the San Andreas fault (e.g., Zoback et al., 1987), as opposed to favoring Byerlee rock strength. Our choice of parameters in the slip-weakening model results in shear stress on the order of 60 MPa at the hypocentral depth, consistent with previous studies (Schmedes et al., 2010). The parameters of the rate-and-state model incorporate failure consistent with Byerlee rock strength.

We define the resulting slip-weakening frictional parameters μ_s and μ_d to obtain an average S ratio (ratio of the peak strength minus the initial stress to the initial stress minus the residual strength) of 2.0 over the fault plane. In addition, we chose the slip-weakening distance D_c to ensure that we resolve the breakdown zone at the crack tip by at least five nodes for the majority of the rupture. In all simulations (including rate-and-state), the frictional coefficients remain constant over the velocity-weakening portion of the fault. Even though the distributions of frictional coefficients are constant, the resulting distributions of material strength are heterogeneous due to fault roughness.

For each set of input parameters, we nucleate ruptures on 32 rough faults. We include stochastic roughness down to a minimum wavelength of $\lambda_{min} = 4 dx$ or 100 m. This results in equivalent scale lengths for the cohesive zone and roughness wavelength, which is near the resolution limit where the rupture will be able to interact with the shortest wavelengths. Fault roughness is described using a dimensionless parameter $\alpha = h_{rms}/L$, where L is the length of the fault, and h_{rms} is the RMS roughness of the 2-D fault profile. We include faults using $\alpha = [0.005, 0.007, \text{ and } 0.009]$ in our database.

We follow the approach of Fang and Dunham (2013) to choose the hypocenter locations on each rough fault. For each fault, we smooth the initial friction $\mu_0 = |\tau_s|/\tau_n$ using a Gaussian kernel with a window-length of 2.5 km, roughly corresponding to the critical radius for spontaneous rupture. We define the hypocenter as the region having smoothed $\max(\mu_0)$, where the fault is closest to failure. Hypocenter locations are chosen between 5 and 10 km depth, and are restricted to being at least 5 km from the edge of the fault. Even though we attempt to simulate 32 separate models for each set of input parameters, the rough fault can prohibit nucleation and spontaneous rupture. In this case, we discard the model and do not include the rupture in our database and subsequent analysis. In addition, we consider only one set of hypocenters for each rough fault realization.

2.1.4. Plasticity and Velocity Strengthening

Studies have shown that rough-fault simulations can require plasticity to eliminate large concentrations of stresses around geometric complexities on the fault (Dunham et al., 2011), especially when using strongly rate-weakening friction laws. For the rate-and-state models, we assume a material cohesion of 5 MPa and an internal friction coefficient $\tan(\phi) = 0.75$ following Shi and Day (2013). We also include plasticity in one ensemble of slip-weakening models. For these slip-weakening models we use a cohesionless material and internal friction coefficient $\tan(\phi) = 0.45$ to be consistent with the material strength defined by the static friction coefficient $\mu_s = 0.4$ in those models. The cohesionless yield surface prevents tensile stress state on the fault plane, which effectively prevents fault opening (Dunham et al., 2011). We note that a cohesionless yield surface in some cases may produce overestimation of plastic yielding and reduction in physical source fields near the free surface. At depth, this effect becomes minimal.

In the slip-weakening models including plasticity, we do not artificially emulate velocity-strengthening behavior near the free-surface. We allow the reduced elastic parameters from the 1-D velocity model along with the plastic deformation to approximate the energy-absorbing behavior of rupture at the free-surface. However, rate-and-state friction allows us to control the rate-weakening behavior of the model. We adjust the a and b parameters to cause velocity-strengthening above $z = -4$ km following Shi and Day (2013); effectively, only $z > -1.5$ km has parameters $a - b < 0$. Finally, for the elastic slip-weakening models, we emulate velocity-strengthening by adjusting the dynamic coefficient of friction μ_d to be equal to μ_s , following Ma and Andrews (2010). This velocity strengthening behavior reduces the resulting ground motions, producing results in better agreement with observations, including observed differences between surface-rupturing and buried rupture models by Pitarka et al. (2009) and Dalguer et al. (2008).

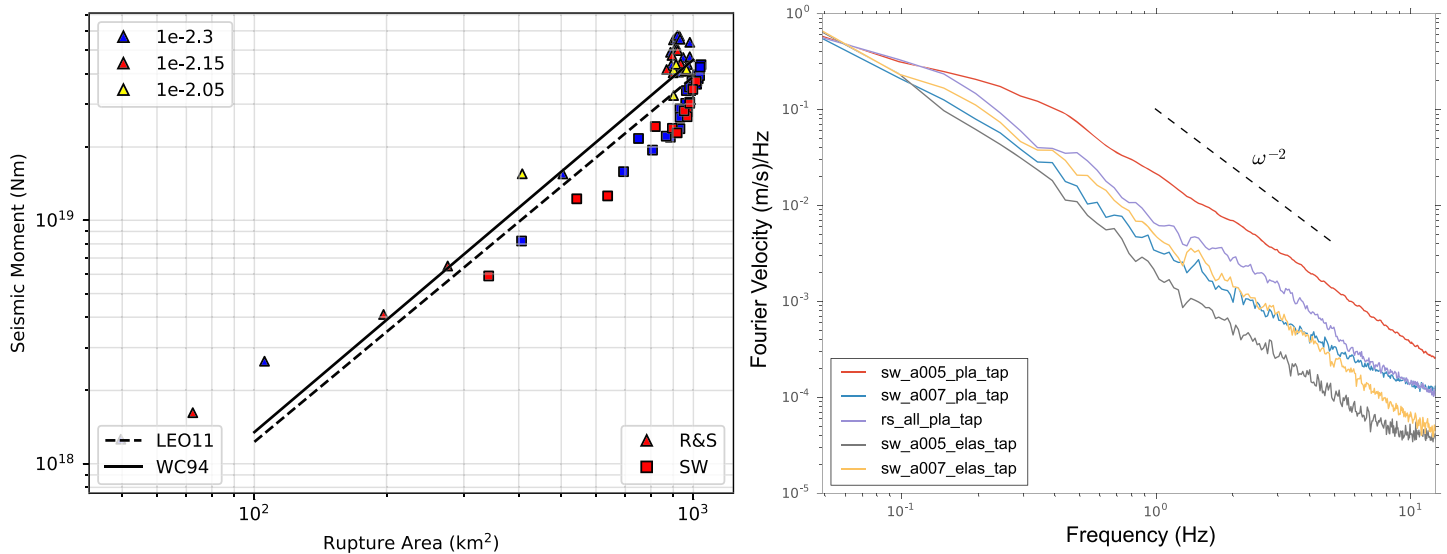


Figure 1. (left) Moment versus area-scaling relationships from the dynamic rupture ensemble, plotted against empirically derived models for inter-plate strike-slip events (Leonard, 2010, “LEO11”; Wells & Coppersmith, 1994, “WC94”). We distinguish between fault roughness using color (blue: $\alpha = 0.005$; red: $\alpha = 0.007$; and yellow: $\alpha = 0.009$) and the friction law using shapes (triangle: rate-and-state; square = slip weakening), where α is the RMS of the rough fault profile normalized by fault length ($h_{rms} L^{-1}$). (right) Stacked source spectra computed from finite fault moment rate functions for all five dynamic ensembles. Each colored line represents an ensemble average computed across all realizations in the ensemble. We normalize all spectra to unit variance before stacking. The dashed black line depicts the ω^{-2} high-frequency decay.

2.1.5. Nucleation

In all of the slip-weakening models, we use a forced-rupture technique to nucleate rupture on the rough faults. The fault is forced to rupture at a fixed velocity of $0.7 V_s$ over a critical distance which depends on the slip-weakening parameters and initial stress. This produces a gradual nucleation when sufficient stress intensity has accumulated at the crack tip to promote spontaneous rupture. In the rate-and-state models, we cannot force the nucleation using the same approach. Instead, we apply a perturbation in shear stress at the hypocentral location, which is typically 5–10 MPa greater than the peak-strength, τ_p . We calibrate the initial stress perturbation to ensure that unnecessarily large nucleation phases did not contaminate the solution.

2.2. Ensemble Overview

We simulated 108 events on rough faults, including different initial parameterizations in an attempt to capture the epistemic uncertainty associated with the dynamic rupture problem. We chose end-member cases of initial conditions to produce rupture models that would, on average, reproduce the characteristics of models previously published in the literature. Also, unless specified otherwise, we treat each rupture model as having an equal likelihood of occurrence. In effect, this means we compute a single set of one-point statistics and two-point statistics that are representative of all ruptures in our database and combine assuming equal weight to each simulation.

Our goal is a kinematic rupture generator that produces realistic broadband ground motions, consistent with observations. We compare our dynamic rupture simulations against empirically derived moment-area scaling relationships (Hanks & Bakun, 2014; Leonard, 2010; Wells & Coppersmith, 1994) to show that our database produces realistic rupture models. Figure 1 (left) shows the dynamic rupture simulations follow the trend of two moment-area scaling relationships for intraplate strike-slip earthquakes. To produce this figure, we estimate the rupture area assuming a rectangular rupture geometry to maintain consistency with the empirical scaling relationships. Scaling relationships generally assume that ruptures have a rectangular geometry such that $A = LW$, where L is the rupture length and W is the rupture width. Many of our dynamic rupture models have complex rupture geometries that are poorly reflected using this simplified assumption. Thus, the approach to estimate the fault area can significantly impact the estimated rupture area. We find that the estimated rupture areas can vary by up to a factor of 2 when comparing a tight-fitting polygon estimate against the rectangular estimate. Brown et al. (2015) commented on the importance of estimating

rupture area and suggested that using a fraction of the maximum slip could be used to determine the rupture area. We estimate rectangular rupture areas by independently determining L and W such that the slip outside the estimated rupture area does not exceed a threshold value of 0.25 m. This value corresponds to roughly 10% of the average peak slip considering all ruptures in the database. This eliminates nodes where ruptures are artificially terminated by the fault boundaries.

In addition to comparing our database against moment-scaling relationships, we expect source spectra computed from ruptures in our database to follow an approximate ω^{-2} high-frequency decay in spectral behavior described by Brune (1970). Figure 1 (right) shows stacked spectra for the five different ensembles considered in this study. We compute the moment rate function on the fault using $\dot{M}_0(t) = dx^2 \mu(\mathbf{x}) \int \dot{s}(\mathbf{x}, t) d\Sigma$, where $\dot{s}(x_1, x_2, t)$ is the slip rate function at point \mathbf{x} , $\mu(\mathbf{x})$ is the shear-modulus at \mathbf{x} , and dx^2 is the area of the subfault. The integral is computed at each time step for the duration of the rupture. We normalize all spectra to unit variance before stacking to account for ruptures with different moment magnitudes. We find that all ensembles generally follow the ω^{-2} trend, implying that far-field acceleration spectra follow an ω^0 trend up to $f_{max} = 10.0$ Hz, as expected from observations.

3. Overview of Kinematic Rupture Generator

A finite-fault kinematic earthquake source can be defined as a collection of discrete subfaults, each having an individually defined slip history. Within the finite fault, each subfault has its evolution of slip prescribed through a chosen slip rate function.

3.1. Source-Time Function

We use the regularized Yoffe slip rate function (Tinti et al., 2005) in our KRG formulation. The regularized Yoffe function provides an appealing choice due to the empirical connections made to dynamic rupture models (Tinti et al., 2005; Tinti et al., 2009) and the theoretical basis of the Yoffe function (Yoffe, 1951). The regularized Yoffe slip rate can be expressed as

$$\dot{s}(t) = \Delta u \int_{-\infty}^{\infty} g(t-T)y(t) dT, \quad (1)$$

where

$$g(t) = \frac{1}{\tau_s^2} [tH(t)H(\tau_p - t) + (2\tau_s - t)H(t - \tau_s)H(2\tau_s - t)],$$

and

$$y(t) = \frac{2}{\pi\tau_r} H(t)H(\tau_r - t)\sqrt{\tau_r - t}.$$

Here, H is the Heaviside function and t is time. The parameters Δu_{kin} (final slip of kinematic source function), τ_s (peak time), τ_r (rise time), and t_0 (rupture initiation time) are needed to completely define the regularized Yoffe function (Figure 2, left).

3.2. Background on Kinematic Source Generation

Our kinematic rupture generator uses statistics computed from dynamic rupture simulations along geometrically rough faults to simulate spatial fields reflecting the dynamic rupture models. The simulated spatial fields are related through empirical relationships to the parameters of the regularized Yoffe function. These spatial distributions of parameters define the source-time function on each subfault, which completely describes the kinematic finite-fault source in both space and time. Thus, the KRG operates conceptually in two different phases.

First, we simulate the physical spatial fields: Δu (final slip), peak slip velocity (v_{peak}), and rupture velocity (v_{rup}) normalized by the local shear wave velocity (c_s) (v_{rup}/c_s) based on the one- and two-point statistics computed from dynamic rupture simulations along rough faults. The v_{rup} is calculated by determining the rupture time between two adjacent ruptured nodes. Second, we compute the parameters of the regularized

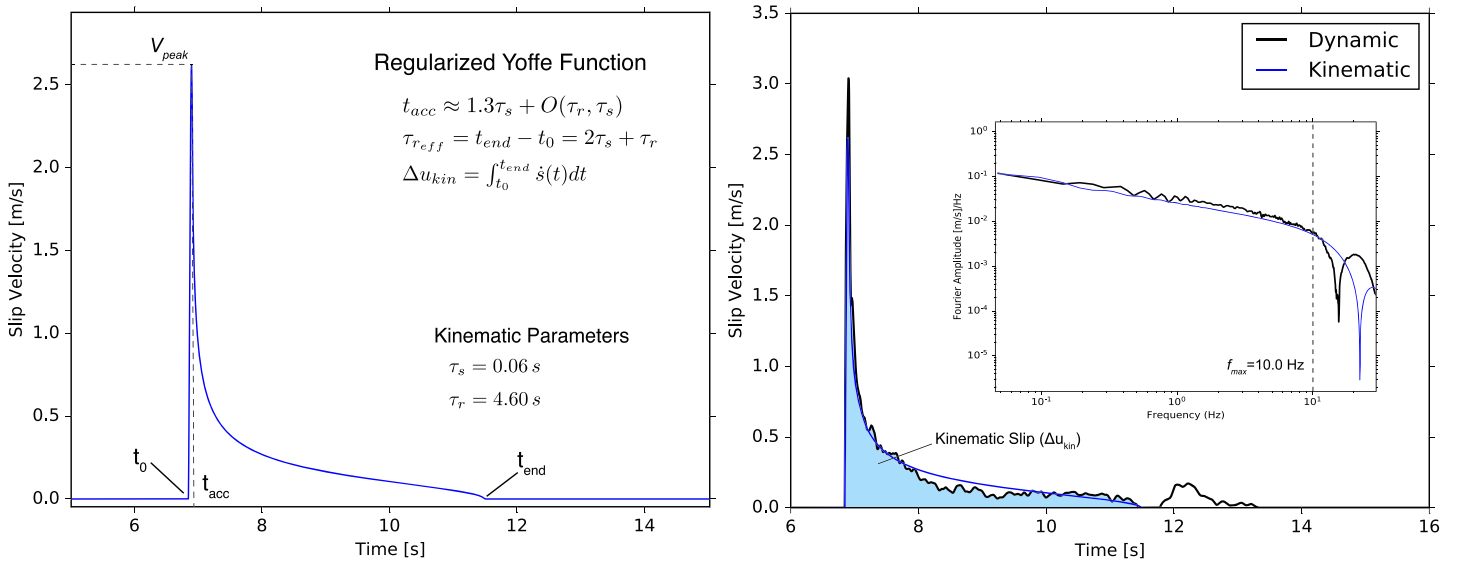


Figure 2. (left) Regularized Yoffe function calculated using $\tau_s = 0.06$ s and $\tau_r = 4.60$ s. In addition, we show useful definitions relating the kinematic parameters to characteristics of the source-time function. (right) Dynamically computed slip rate function (black) and best fitting kinematic approximation (blue). The shaded region under the dynamic function depicts the kinematic slip, which does not include afterslip. The inset of the figure shows the comparison in the frequency domain. In the inset, the dashed line represents the target frequency of our KRG.

Yoffe function (t_0, τ_r, τ_s) using empirical relationships defined between the simulated physical fields and these kinematic parameters.

Two recent studies by Trugman and Dunham (2014) and Yao (2017) investigated spatial correlations between rough fault topography and physical spatial fields using dynamic ruptures along rough faults. In the 2-D case, Trugman and Dunham (2014) found that $\Delta u, V_{peak}$, and v_{rup}/c_s were strongly correlated with the local slope of the rough fault topography. However, for 3-D, we follow Yao (2017) who found that the physical source fields are correlated with the initial friction (μ_0) or the ratio of shear traction to normal traction on the fault. The 2-D and 3-D results are consistent in the sense that μ_0 represents a proxy for the initial fault slope. These relationships constitute a physical basis for the relationship between the rough fault topography and the resulting rupture process.

To describe the spatial interdependency noticed by Trugman and Dunham (2014) and Yao (2017), we define a 4-D Gaussian random variable consisting of $\Delta u, V_{peak}, v_{rup}/c_s$, and μ_0 having its spatial correlation defined by a linear model of coregionalization (LMC). LMCs produce outputs as linear combinations of independent random functions with the resulting covariance function being positive semidefinite. In the supporting information to this article, we provide a brief background on LMCs, sequential simulation of random variables, and list some advantages and disadvantages over using empirically defined correlation structures (e.g., Song et al., 2013).

3.2.1. Simulating the Physical Source Fields

With the theoretical background covered in the supporting information, we provide an overview of the general steps to simulate the physical source fields used in our rupture generator: $\Delta u, V_{peak}$, and v_{rup}/c_s . This process is known as Sequential Gaussian Simulation and follows Goovaerts and Goovaerts (1997):

1. Simulate a rough fault model following approach outlined in Shi and Day (2013) and compute the initial friction using $\mu_0 = |\sigma_s|/\sigma_n$. We assume the same background stress model used in the dynamic rupture computation to estimate μ_0 , although in theory any sensible model could be used.
2. Define a finite fault, A , along with a random path traversing A that visits each node u' only once.
3. At each u' in A , compute the mean and variance of the Gaussian conditional cumulative distribution function using Equations (S13) and (S14). The cokriging system is solved using the spatial correlation model defined by the LMC described in the supporting information.
4. Sample the conditional cumulative distribution function using the parameters obtained in the previous step (Equation S12), and add $y_i(u')$ to the data set.

5. Advance to the next node and complete the previous two steps. Repeat until all nodes are simulated.
6. Apply transformation of the simulated normal scores into the simulated values $z_i(\mathbf{u}')$ using the reverse of the process shown in Equation (S10).

This framework provides flexibility to improve future versions of the kinematic rupture generator. For example, more sophisticated kriging estimators can be applied to capture specific dynamic effects in addition to different models of the spatial correlation structure. In addition, the conditional simulation approach allows us to include other information, such as a model of Δu constrained by finite-fault inversions or dynamic rupture simulations.

4. Extracting Statistics for Kinematic Source Generation

4.1. Data Preparation

We apply a preprocessing routine to the computed dynamic rupture models before extracting any statistics, consistent between all ensembles and applied to each simulation in the ensemble. This process involves eliminating undesirable points that should not be included in the analysis. We eliminate points based on Boolean criteria using a logical masking procedure. First, we exclude all subfaults at depths $z > 15$ km and $z < 4.0$ km, representing points that rupture within velocity-strengthening regions on the fault. Next, we mask all points falling within a circle having radius = 4 km and its origin at the hypocenter. Due to the artificial nucleation of dynamic rupture simulations, the points directly affected by the nucleation technique are not included in the analysis. We also exclude points with $V_{peak} < 0.1$ m/s, because we are interested in computing statistics for subfaults that rupture spontaneously and contribute significantly to the moment, M_0 . Finally, we only consider points with subshear rupture velocities in this analysis ($v_{rup}/c_s < 1$), and save supershear propagation for important future work.

Next, we extract one-point and two-point statistics of the dynamic rupture models. One-point statistics refers to statistics that can be computed using a family of singular values, such as the mean or median. As such, two-point statistics are those that must be computed using two points, for example, variance or covariance.

4.2. Fitting Kinematic Slip Rate Functions

In addition to knowing the spatial structure of the physical fields computed during the dynamic rupture (i.e., Δu , V_{peak} , and v_{rup}/c_s), we need to understand how these physical fields relate to the kinematic parameters of the regularized Yoffe function (Equation 1). The parameters of the regularized Yoffe function are the peak time, τ_s , the rise time, τ_r , the kinematic slip, Δu_{kin} , and the rupture initiation time, t_0 . We can recover the kinematic parameters at each subfault by fitting the dynamic slip rate function with the function shown in Equation 1. The recovered kinematic parameters Δu_{kin} and $\max(V_{peak})$ are different than their dynamic counterparts. Hence, we make the distinction between the two sets of parameters when necessary by using this notation.

Finding the best fitting regularized Yoffe function for each dynamic slip rate function requires a straightforward optimization on each subfault. In our database, every dynamic rupture model has ~2 million subfaults ($n_x = 2,601$, $n_z = 801$) and 10,001 time steps ($dt = 0.002$ s). Due to the high-frequency behavior of the simulations, that result in small values of τ_s , we have to fit slip rate functions without downsampling the simulation output. Due to the size of the three-component slip rate function outputs, we determine the kinematic slip rates for a single ensemble of slip-weakening simulations. In total, we analyzed ~4 TB (about 80 million subfaults) of slip rate functions for determining the kinematic parameters.

We fit the parameters of the regularized Yoffe function in two separate steps. In the first step, we determine parameter values that can be directly computed from the dynamic slip rate functions. Then, we use these values along with a grid search optimization routine to estimate the remaining parameters. First, we determine t_0 directly from the dynamic slip rate function. Following the approach of Mai et al. (2017) and Schmedes et al. (2013), we define a time t_{end} where the slip reaches zero for the first time. We then compute the kinematic slip using $\Delta u_{kin} = \int_0^{t_{end}} \dot{s}_{dyn}(t) dt$, where $\dot{s}_{dyn}(t)$ is the dynamic slip rate function, which provides more accurate recovery of the dynamic V_{peak} . Using the computed parameters t_0 and Δu_{kin} , we optimize a least squares cost function to determine the best fitting values of τ_r and τ_p on each subfault. We note that simply estimating the rise time using $\tau_r = t_{end} - t_0$ produces an incorrect estimate of τ_r , since

$\tau_{\text{reff}} = t_{\text{end}} - t_0 = 2\tau_s + \tau_r$ (Tinti et al., 2005), which results from the convolution of the Yoffe function with parameter τ_r and the triangular function with half-length τ_s .

Figure 2 (right) shows a typical dynamic slip rate function with the best fitting regularized Yoffe function. We find that the regularized Yoffe function provides a good approximation to the dynamic slip rate functions, and sufficiently recovers the frequency content in the dynamic simulations.

4.3. One-Point Statistics

The Sequential Gaussian simulation technique operates under the parametric assumption of a multivariate Gaussian random variable. This means that simulated field values are initially defined as quantiles of a standard normal variable. In order to recover the desired one-point statistics, a normal-score transform must be applied to the simulated data. Several studies have shown that one-point statistics of dynamic rupture models are non-Gaussian. For example, Schmedes et al. (2010) and Song et al. (2013) analyzed ruptures on flat faults and show depth dependence in the marginal distributions of one-point parameters in addition to a dependency on hypocentral distance. However, a recent study on the statistics of rough faults by Yao (2017) showed that sufficiently rough faults (α larger than about 0.005) eliminate the dependency on the distance to the hypocenter. We find similar results to Yao (2017) in our dynamic rupture database, and therefore do not include any distance dependence of the marginal PDFs (mPDF) in our KRG.

After simulating the rupture fields using sequential Gaussian simulation, we transform the k th largest value from the simulated standard normal distribution with the k th largest value observed in the functions (Figure 3). The mPDFs are subject to the limitations of the dynamic ruptures computed for our analysis. In other words, we cannot say that these mPDFs would represent the distributional statistics observed for arbitrary rupture mechanisms or magnitude, but they are representative of the M_w 6.4 to M_w 7.2 ruptures on strike-slip faults considered in this study.

Due to the limitations of simple kriging (i.e., the assumption that the mean is known), we only consider regions on the fault that do not display a trend as a function of depth. This allows us to compute residuals using a scalar mean value and use simple kriging, as the mean value is known to be zero for the residual fields. Thus, we focus on the region between $4 \text{ km} < z < 15 \text{ km}$ where the rupture fields display a reasonably constant mean as a function of depth. Above 4 km, we apply a linear tapering based on these results and those obtained by Xu et al. (2016) relating to shallow slip deficit (see Figure 4).

4.4. Two-Point Statistics

Estimating regionalization models poses minor challenges in the multivariate case. These challenges arise from the limitations inherent with linear models of coregionalization where both semivariograms and cross-semivariograms must be described by semivariogram models with equal range parameters. In practice, this results in a trade-off between the semivariogram estimates for direct and cross semivariogram estimates within the linear model of coregionalization, with better fits for certain semivariograms and worse fits for others. In the supporting information, we outline our approach for obtaining the linear model of coregionalization used to represent our dynamic rupture database.

Figure 5 shows the best fitting linear model of coregionalization fit using range parameters $a_s = 250 \text{ m}$ and $a_l = 5000 \text{ m}$. We chose range parameters that best represent both the direct semivariograms in addition to the cross semivariogram with μ_0 . The estimated spatial correlation structure from our dynamic ensemble is shown using the blue circles. The black line depicts our preferred linear model of coregionalization, which we explain below. We define the nested exponential model using equation (S17) which provides the simplest model that represents our semivariogram estimates. For μ_0 and v_{rup} the semivariance seems to be dominated by short scale length processes, and Δu and V_{peak} seem to be controlled by long-scale processes. We attribute the small-scale length process to behavior on the scale length of the breakdown zone, which can explain the small-scale lengths for v_{rup} . The longer correlation length of Δu and V_{peak} is likely controlled by the crack-length or the pulse width of the dynamic rupture simulations.

Table 1 lists the coefficients of the coregionalization matrices \mathbf{B}^l for the short-range and long-range components, respectively. Notice that we do not include a nugget effect (discontinuity at zero lag) in this model. In nearly all the direct and cross semivariogram estimates the value of the semivariogram is near zero at zero lag. Only v_{rup} displays a significant effect at $h = 0$. We also do not consider anisotropy in our LMC, while Mai

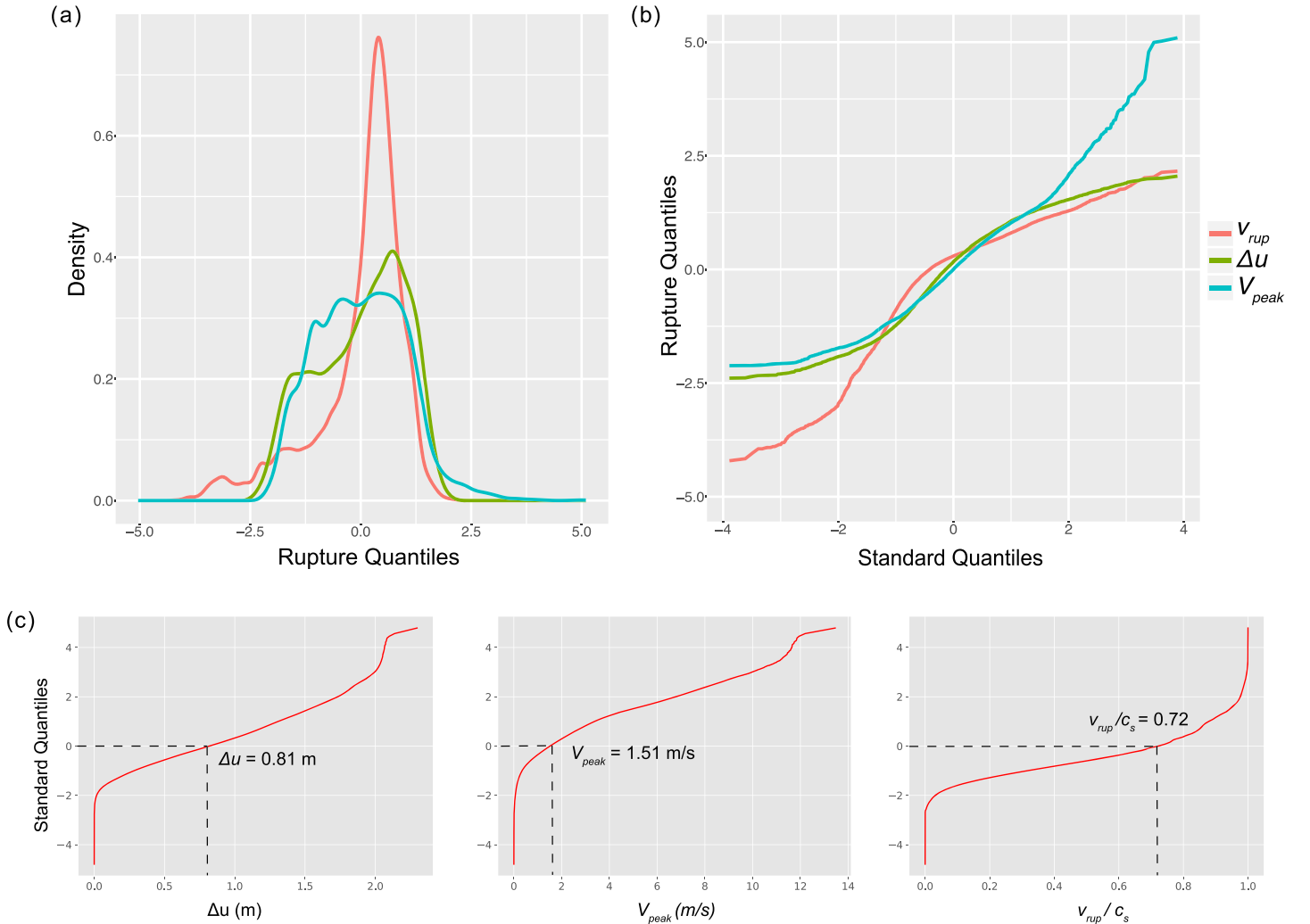


Figure 3. Density functions (a) and quantile-quantile plot (b) shown for normalized physical source fields. The one-point statistics are computed for all dynamic ruptures in our database. We normalize the physical fields by the simulation mean and standard deviation before computing the density function. (c) Mapping from simulated normal-score value to desired physical quantity. These functions preserve the order statistics observed in the dynamic rupture simulations by equating the k th largest simulated value with the k th largest value of the desired marginal probability density function. The median values are depicted on the figure with dashed lines.

and Beroza (2002) find that large strike-slip events display anisotropy, likely due to the aspect ratio of long rectangular faults. Incorporating anisotropy or a more complicated covariance model could be targets for future improvements of the rupture generator.

We can compute the zero-offset correlation matrix at $\mathbf{h} = 0$ based on our linear-model of coregionalization using the relationship $\mathbf{C}(0) = \lim_{h \rightarrow +\infty} \mathbf{\Gamma}(h) = \mathbf{B}^1 + \mathbf{B}^2$, where \mathbf{B}^l are the coregionalization matrices. Table 1 lists the zero-offset correlation from our LMC. We present normalized coregionalization matrices so that the diagonal components of $\mathbf{C}(0)$ equal unity, allowing us to compare our spatial correlation model with the results from Yao (2017). Our values all fall within the distributions of correlation coefficients found in that study, and our preferred linear model of coregionalization reproduces the general features of our dynamic rupture simulations. While we observe correlations for the source parameters, Trugman and Dunham (2014) found much larger correlations between the source fields. The differences are likely due to the more complex rupture behavior in 3-D as opposed to the 2-D simulations used in their study. For example, in 3-D, the fault has the ability to rupture around an asperity whereas a 2-D rupture cannot. This likely explains the lower correlations with μ_0 .

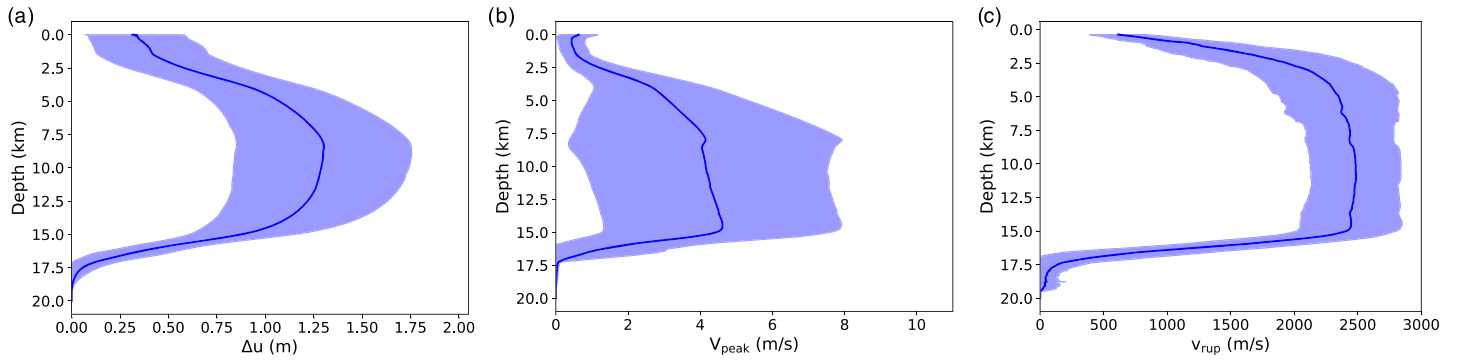


Figure 4. Depth dependency of one-point statistics computed for (a) final slip Δu (b) peak slip velocity V_{peak} , and (c) rupture velocity v_{rup} for all ruptures in our database. The thick blue line depicts the mean value computed at that depth for all ruptures, and the shaded region represents ± 1 standard deviation of the mean value. The near-surface effects of the velocity strengthening imposed in the rupture models are apparent in all of the physical fields. Notice the large variability in V_{peak} as compared with the other rupture fields.

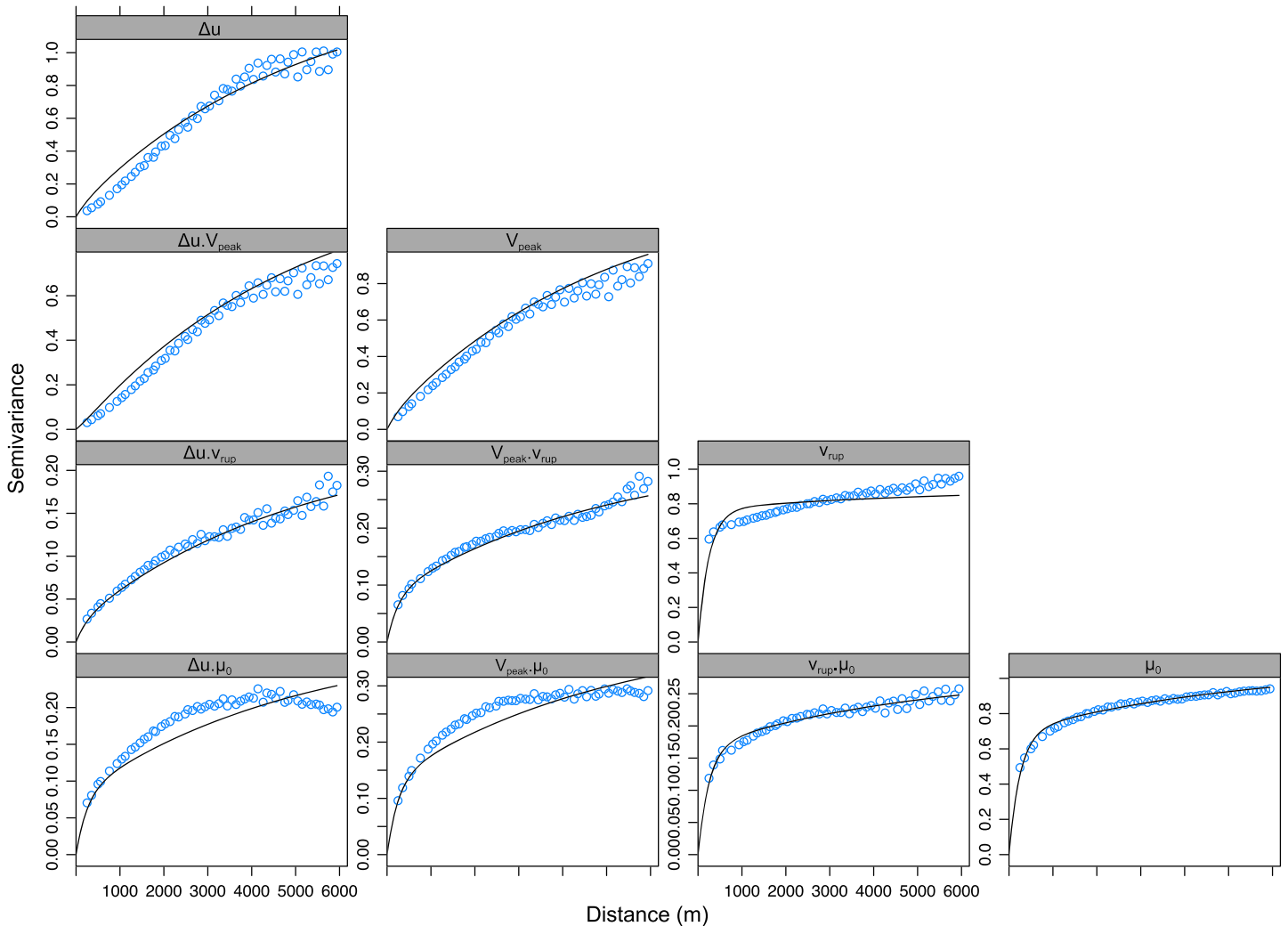


Figure 5. Preferred linear model of coregionalization for the dynamic rupture ensembles. Our model consists of two nested exponential semivariograms with range parameters 250 and 5,000 m. Expected semivariance estimates are shown using blue circles and the corresponding linear model of coregionalization is depicted with a black line.

Table 1
Coefficients of Coregionalization Matrices

Field	Δu	V_{peak}	v_{rup}	μ_0
Short-range coregionalization matrix, \mathbf{B}^1				
Δu	0.0282			
V_{peak}	0.0002	0.0403		
v_{rup}	0.0164	0.0631	0.6917	
μ_0	0.0783	0.1215	0.154	0.6049
Long-range coregionalization matrix, \mathbf{B}^2				
Δu	0.9718			
V_{peak}	0.81	0.9597		
v_{rup}	0.1504	0.1841	0.3083	
μ_0	0.0946	0.15	0.0859	0.3951
Zero-offset correlation coefficients, $C(0)$, between source parameters computed from linear model of coregionalization				
Δu	1			
V_{peak}	0.8102	1		
v_{rup}	0.1667	0.2472	1	
μ_0	0.1729	0.2715	0.24	1

4.5. Empirical Relationships for Kinematic Parameters

We now derive empirical relationships between the parameters of the regularized Yoffe function, namely, the rupture initiation time, t_0 , the peak time τ_s , and the rise time τ_r , and simulated rupture fields, in order to produce a complete kinematic slip model.

4.5.1. Rupture Initiation Time

When computing the rupture initiation time, t_0 , we first scale the simulated v_{rup}/c_s by the c_s of the ground motion simulation to produce v_{rup} (m/s). Next, we define a hypocenter location on the finite-fault plane. Using a fast-marching solution to the Eikonal equation, we convert the simulated v_{rup} into rupture initiation times t_0 for each subfault.

4.5.2. Peak Time

Using laboratory experiments, Ohnaka and Yamashita (1989) proposed the relationship $V_{peak} \propto D_c f_{max}^s$, where D_c is the critical slip-weakening distance, and f_{max}^s represents the cutoff frequency of the slip rate function. Tinti et al. (2005, 2009) confirmed that this relationship holds for the regularized Yoffe function used in our KRG. Using the data in Table 1 of Tinti et al. (2005),

$$\tau_s \approx \alpha_0 \frac{\overline{d'_0}}{V_{peak}}, \quad (2)$$

where α_0 is a constant of proportionality. We replaced D_c with d'_0 in Equation 2, because the notion of D_c does not translate directly to a kinematic source time function. We can regard d'_0 as a value that can be directly computed from the parameters of the regularized Yoffe function (Tinti et al., 2005). Tinti et al. (2005) showed that one can relate the kinematic parameters τ_s , τ_r , and Δu to d'_0 using:

$$d'_0 \approx \Delta u \sqrt{\frac{1.3\tau_s}{\tau_r}}, \quad (3)$$

Using Equation 3 we estimate d'_0 for 16 simulations randomly selected from our ensemble. The chosen simulations share a value of $D_c = 0.16$ m, and we recover an average value of $d'_0 = 0.13$ m. Using this estimate of d'_0 , we compute the coefficient $\alpha_0 \approx 1.55$ by performing a least-squares estimate on Equation 2.

Here, we summarize the process to estimate the variable τ_s on the fault given the simulated spatial field V_{peak} : (1) assume a target f_{max}^s for the kinematic source model and compute the value of d'_0 corresponding to the chosen f_{max}^s using the relationship $\overline{V_{peak}}/d'_0 \approx 2.5 f_{max}^s$, which comes from rearranging the empirical relationship from Ohnaka and Yamashita (1989). The overbar denotes the average V_{peak} of the simulation. We determine the constant of proportionality using the least squares fit to the data shown in Figure 6a. (2) Compute τ_s for each subfault using the the V_{peak} simulated on that subfault and d'_0 computed in Step 2 (Equation 2; Figure 6b). By applying this two-step process instead of simply regressing on Equation 2, we expose f_{max}^s as a parameter to use in the kinematic model.

In order to prevent unrealistically large values of τ_s , we have implemented empirical rules to define the effective V_{peak} derived from the dynamic rupture simulations. First, we limit the ratio between simulated Δu and V_{peak} to 2 to eliminate areas on the fault with large Δu , but low V_{peak} . Next, we limit the $\min(V_{peak})$ to 0.1 m/s to prevent unrealistically large values of τ_s . The choices of these rules are largely arbitrary, but produce distributions of τ_s consistent with those computed from the dynamic rupture simulations.

4.5.3. Rise Time

Finally, we need to calculate τ_r before we can generate our finite-fault kinematic slip model. Guatteri et al. (2004) proposed that the effective rupture duration t_{dur} relates linearly to the total slip duration on a given subfault (τ_{reff}). In our dynamic rupture models, $\tau_s \ll 1$, indicating that $\tau_r \approx \tau_{reff}$, so the relationship proposed for the triangular source time function used by Guatteri et al. (2004) should apply here. In addition, we know

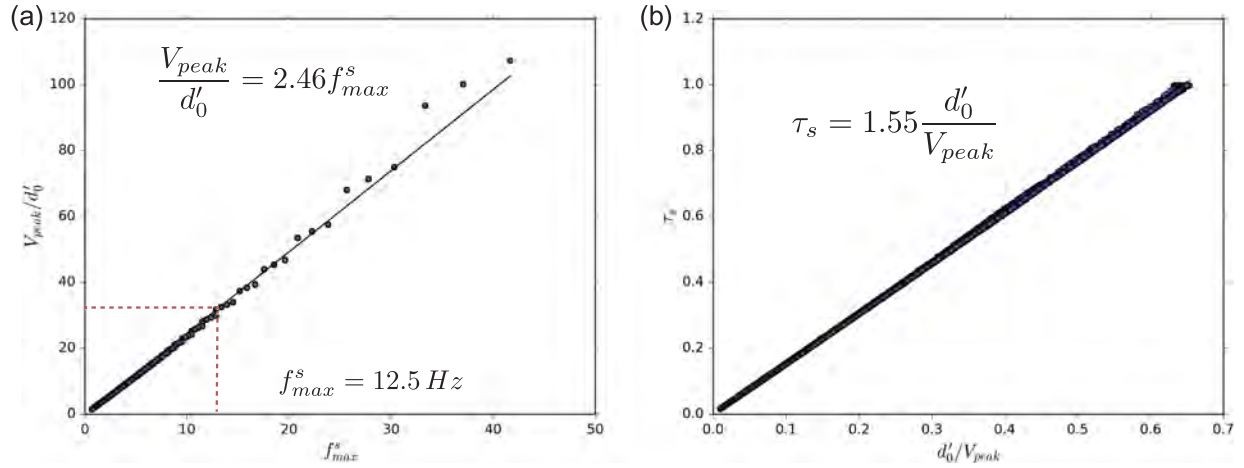


Figure 6. Outline of the two-step procedure to estimate τ_s from the physical source fields. (1) By choosing an arbitrary f_{max}^s , we can compute the d'_0 associated with this f_{max}^s by using the average V_{peak} for the simulation and applying the relationship shown in (a). (2) using the estimate of d'_0 we calculate the corresponding value of τ_s assuming the subfault V_{peak} using the relationship shown in (b). This process produces spatially variable τ_s with average f_{max}^s chosen in Step (1).

that Δu correlates with τ_r from previous studies (e.g., Schmedes et al., 2010; Yao, 2017). Therefore, we construct a linear model using the final slip Δu and effective rupture duration t_{dur} as predictors to estimate τ_r . This relationship is defined using the following:

$$\tau_r = \beta_0 \Delta u + \beta_1 t_{dur}, \quad (4)$$

where the coefficients β_0 and β_1 are found to be 3.55 and 0.08, respectively. We also investigated the possibility of an interaction between Δu and t_{dur} , but do not obtain passable models for predicting τ_r , when including the interaction term in Equation 4. Figure 7 shows the predictions of this model compared with the results from dynamic rupture simulations with scatter plots for each predictor (Δu and t_{dur}) plotted against τ_r by fixing the value of the predictor to its mean value in Figure 7.

Finally, t_{dur} must be specified in order to compute τ_r using Equation 4. We define t_{dur} for a simulation by using the average value of t_0 on the fault boundary. Subfault locations that have negative t_{dur} (i.e., subfaults that rupture after the chosen t_{dur}) are not permitted to rupture by setting $\Delta u = 0$.

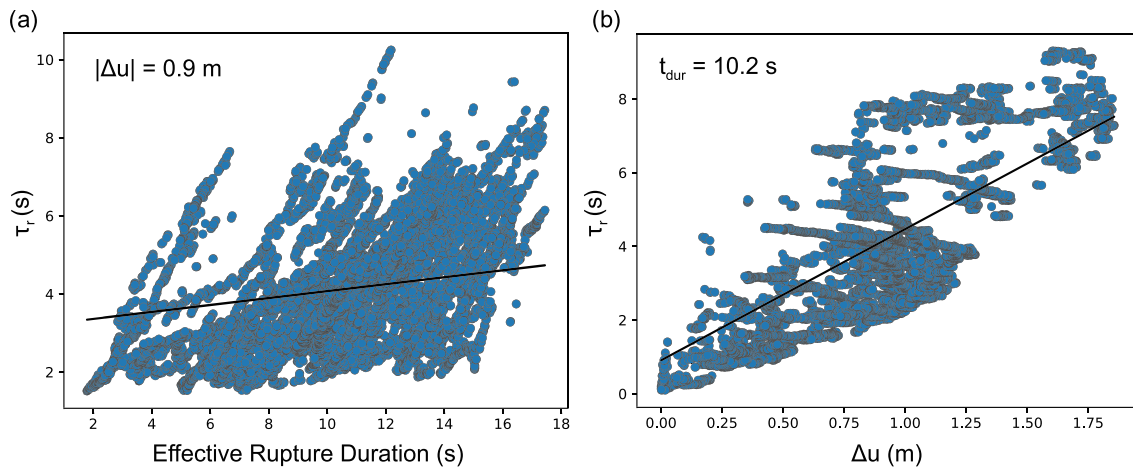


Figure 7. Multiple linear model defined to estimate τ_r given the final slip Δu and the effective rupture duration t_{dur} . (a) τ_r as a function of t_{dur} for subfaults where $\Delta u = 0.9 \text{ m} \pm 0.001 \text{ m}$. The black line shows the predicted values of τ_r . (b) τ_r as a function of Δu for subfaults where $t_{dur} = 10.2 \text{ s} \pm 0.01 \text{ s}$, the black line shows the predicted τ_r .

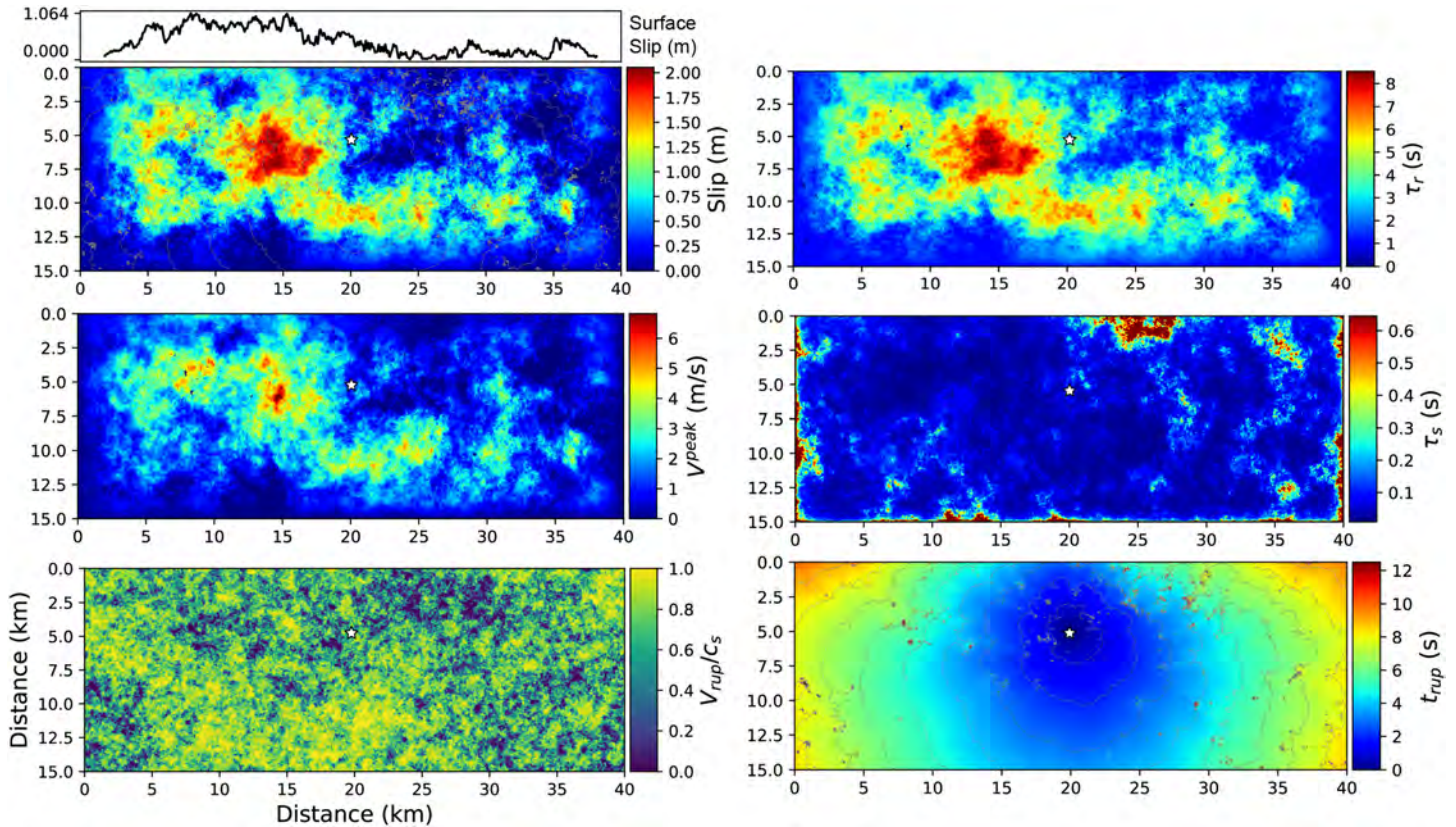


Figure 8. Example kinematic source model generated using methodology presented in this paper. The kinematic parameters Δu , τ_s , τ_r , and t_0 completely describe the spatiotemporal evolution of slip on the fault using the regularized Yoffe function. We show the corresponding V_{peak} and v_{rup}/c_s associated with the kinematic parameters. The yellow star depicts the hypocenter location set at $x = (20 \text{ km}, 5 \text{ km})$.

4.6. Sample Kinematic Rupture Realization

Figure 8 shows an example kinematic source generated using the methodology described in this paper. We can see the correlation between τ_r and Δu in addition to the anticorrelation between V_{peak} and peak time τ_s . In addition, the variability in v_{rup}/c_s results in the rough distribution of rupture initiation times t_0 . In the next section, we present ground motions computed using finite-fault sources generated using this methodology.

5. Validating the KRG

The validation procedure can be considered an impossible task for natural systems (Oreskes et al., 1994), but nonetheless it is imperative to display that models provide useful and sensible results. In this context, we are interested in understanding the usefulness of this KRG implementation to generate broadband seismic sources that produce reasonable ground motion amplitudes and variability. We constrain the validation of the KRG to ground motions within 25 km from the finite fault where effects from anelastic attenuation or scattering are limited.

We validate the ground motions produced using sources from the kinematic rupture generator described in this paper by comparing deterministic simulations against leading GMPEs (e.g., Abrahamson et al., 2014; Boore et al., 2014; Campbell & Bozorgnia, 2014; Chiou & Youngs, 2014). In addition to GMPE comparisons, we show visualizations of far-field acceleration and displacement spectra in addition to seismograms extracted at select stations around the finite fault.

We computed ground motions using the fourth-order space second-order time staggered-grid finite difference code AWP-ODC-CPU (Cui et al., 2010, 2013) including frequency-dependent attenuation (Withers et al., 2015) and perfectly matched layers (Marcinkovich & Olsen, 2003) using 20 nodes to minimize grid

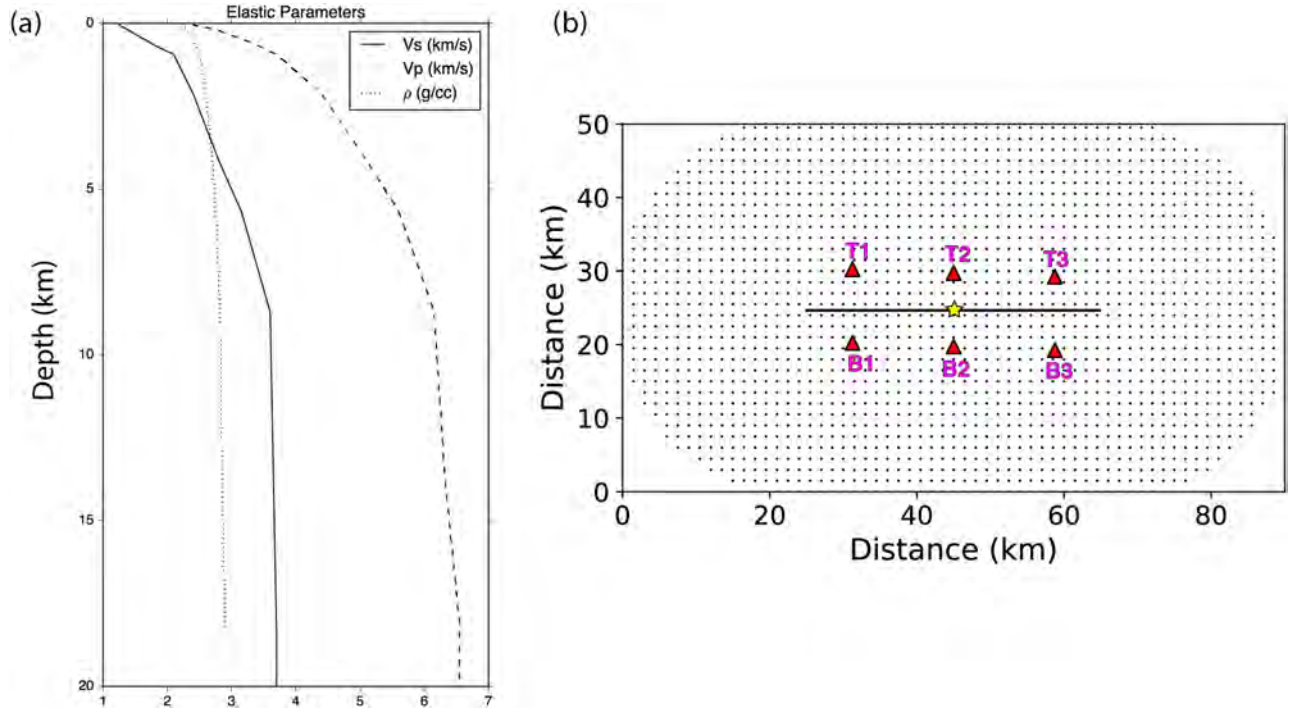


Figure 9. (a) Material model for shear wave velocity (V_s), P wave velocity (V_p), and density (ρ). This model represents a smooth 1-D profile representative of a rock site in southern California based on a 1-D profile extracted from the SCEC CVM-S4.26 velocity model. (b) Free surface of simulation domain showing six stations (red triangles) used for qualitative visualizations of seismograms and spectra. Black dots depict stations used to extract spectral accelerations for GMPE comparisons. The epicenter location is shown using the yellow star.

boundary-reflected energy from contaminating the solution. We refer the interested reader to Cui et al. (2010, 2013) for an in-depth description of the numerical method.

We simulate 40.0 s of deterministic wave propagation in a $90 \text{ km} \times 50 \text{ km} \times 25 \text{ km}$ domain discretized using $dx = 25 \text{ m}$. The simulations run for $\sim 3.5 \text{ hr}$ using 7,200 processors on ORNL Titan. We incorporate a 1-D velocity profile with $\min(V_s) = 1,250 \text{ m/s}$ representative of a hard-rock site (Figure 9), resolving frequencies up to 10 Hz with a minimum wavelength $\lambda_{\min} = 125 \text{ m}$ using at least five points per wavelength. To model anelastic attenuation, we incorporate a linear relationship between Q_s and V_s . For $f > 1 \text{ Hz}$, we model frequency-dependent attenuation using a power law with exponent $\gamma = 0.6$. We express this frequency-dependent attenuation relationship using

$$Q(f) = \begin{cases} Q_0 \left(\frac{f}{f_0}\right)^\gamma, & f \geq f_0, \\ Q_0, & f < f_0 \end{cases} \quad (5)$$

where $f_0 = 1.0 \text{ Hz}$, and $Q_0 = 100 V_s$. Equation 5 provides the shear wave quality factor Q_s , and we represent the P wave quality factor as $Q_p = 2Q_s$.

5.1. Kinematic Source Models for AWP-ODC

We generate five finite-fault kinematic slip models using the rupture generator methodology described above and insert into AWP-ODC via moment-rate components. The strike ϕ_s and dip δ can be computed directly from the rough fault model used to generate the distribution of initial friction μ_0 . Given the fault normal vector $\hat{\mathbf{n}}$ for a subfault, we compute the dip δ as the angle between $\hat{\mathbf{n}}$ and the surface projection ($\hat{\mathbf{n}}_{\text{proj}}$) of $\hat{\mathbf{n}}$ using $\delta = 90 - \cos^{-1}(\hat{\mathbf{n}} \cdot \hat{\mathbf{n}}_{\text{proj}})$, with $\delta = 90^\circ$ corresponding to vertical. In addition, we compute strike using $\phi_s = \cos^{-1}(\hat{\mathbf{n}}_{\text{proj}} \cdot \hat{\mathbf{x}})$, where $\hat{\mathbf{x}}$ denotes the unit vector depicting the Cartesian axis. Lastly, the rake λ is defined using $\lambda = \cos^{-1}(\phi_s \cdot \mathbf{u})$ where ϕ_s denotes the strike-vector and \mathbf{u} denotes the slip vector on the

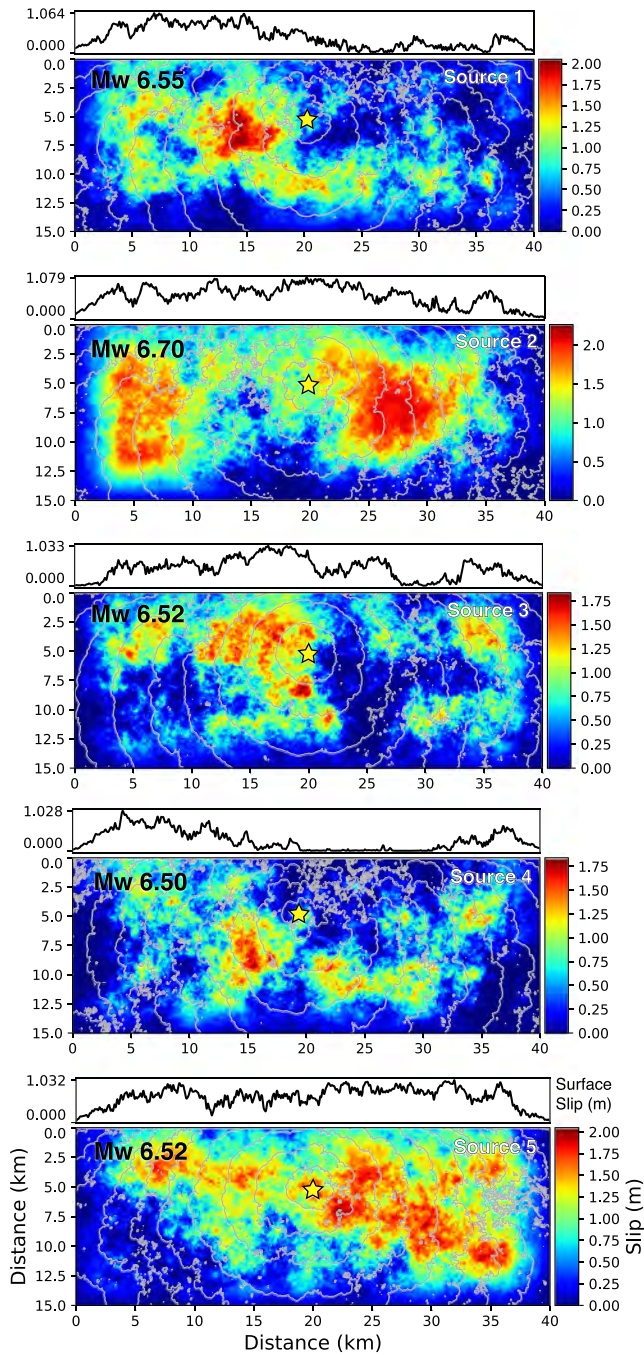


Figure 10. Final slip Δu distributions for five finite fault source models produced using the kinematic rupture generator used for validation. We show the M_w of each earthquake in the upper left of each plot. Contour lines indicate 1 s intervals of rupture initiation times, and we depict the hypocenter location with the yellow star.

fault. In other words, λ represents the angle between fault strike and the slip vector. From our dynamic rupture simulations, we find that λ largely follows ϕ_s with only 10% of subfaults showing $|\lambda - \phi_s| > 1^\circ$, and thus assign $\lambda = \phi_s$.

Figure 10 shows the scalar slip on the fault plane for source models 1–5 considered in the validation. The variation in M_w arises due to the fact that each individual realization from the sequential simulation technique does not necessarily have zero mean, unlike an ensemble of realizations. We generate Δu using the one-point distribution functions shown in Figure 3c. We assign median values to our kinematic sources of $\Delta u = 0.81$ m, $V_{peak} = 1.51$ m/s, and $v_{rup}/c_s = 0.72$, based on dynamic rupture simulations.

The use of these values produces an average slip for the five kinematic sources of 0.64 m (Figure 10). We compare this with the average slip of 1.01 ± 0.38 m from the dynamic ensemble. We note that the kinematic ruptures have an average slip that is approximately 1 standard deviation below the dynamic ruptures. Therefore, while the kinematic sources appear lower than some of the dynamic simulations shown in Figure 1 (left), statistically, they are consistent with the average slip distribution provided by the dynamic simulations. In future versions of the rupture generator, we plan to address this by replacing the empirical distributions (used in this study) with parametric distributions. This change should provide more granular control over the kinematic sources that are generated using this method.

In all of the simulations we project the kinematic model onto a flat fault, but preserve the moment-tensor orientation of the rough fault. This follows the approach of Mai et al. (2017) who showed that projecting moment rates onto a flat fault produces consistent ground motions as long as the moment-tensor components reflect the geometry of the rough fault.

5.2. Ground Motion Validation

Figures 11 and S1 show three-component 0–10 Hz velocity seismograms computed for stations T3 and B3 (see Figure 9b), respectively, 15 km from the epicenter in the along-strike direction and 5 km from the fault plane. These figures show that seismograms originating from the KRG sources produce ground motions that pass the “eyeball” test. In other words, these synthetic records could be mistaken for recorded broadband ground motions without any other context.

Figure 12 shows the corresponding far-field fault-normal acceleration, with amplitudes that increase up to a corner frequency f_c and display flat spectra to $f_{max} = 10$ Hz (following the ω^{-2} source model). This behavior has been observed in natural earthquakes (e.g., records from the 1980 Mexicali earthquake shown by Anderson & Hough, 1984) and published dynamic rupture simulations on rough faults (e.g., Dunham et al., 2011; Shi & Day, 2013). Figure S2 shows normalized Fourier amplitude of displacement computed at the six stations shown in Figure 9b for Source 3.

We show that our rupture generator produces far-field displacement spectra with ω^{-2} high-frequency decay up to the simulated $f_{max} = 10$ Hz, consistent with theoretical considerations for shear failure on faults (e.g., Brune, 1970). We find identical behavior for the high-frequency decay in far-field spectra from the other four kinematic source models considered here.

It is important to verify whether the simulated amplitudes and variability are comparable with spectral accelerations predicted by GMPEs. Figure 13 shows a comparison between 5%-damped GMRotD50



Figure 11. Velocity seismograms plotted for five source models (Sources 1–5) at station T3 (see Figure 9b). The peak motions for each component are shown above the time series. The synthetic seismograms are labeled by their respective source model (see Figure 9).

spectral accelerations (Boore, 2006) for source models 1, 2, and 3 and GMPEs derived from the NGA West2 database (i.e., Abrahamson et al., 2014; Boore et al., 2014; Campbell & Bozorgnia, 2014; Chiou & Youngs, 2014) for periods between 2.0 and 0.2 s at stations located on a 500 m × 500 m grid (see Figure 9b). We find that our source models produce comparable fits with the GMPE medians and display ground motions that fall within ± 1 intraevent standard deviations. Furthermore, we find that all five kinematic source models as a function of distance are unbiased compared to the GMPEs (residuals within 1σ , Figure 14). Additionally, it is noteworthy that our rupture generator produces ground motions with variability consistent with observed earthquakes.

6. Discussion

While the comparison of spectral accelerations from the KRG to those from leading GMPEs by no means represents a systematic validation of the KRG, it provides a promising indication that this model could

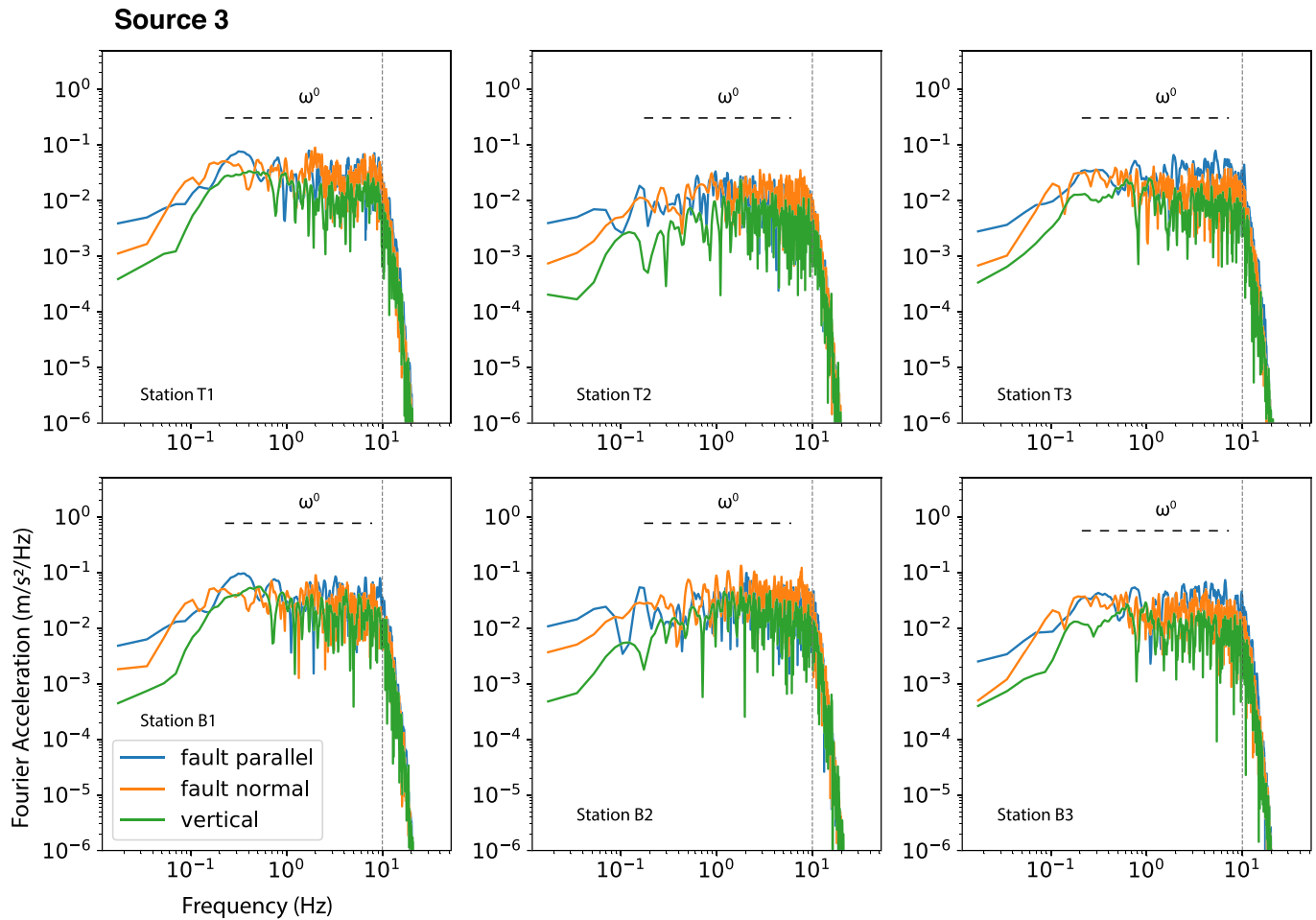


Figure 12. Far-field acceleration spectra computed for Source 3. The vertical dashed line depicts the $f_{max} = 10$ Hz of our deterministic simulations, and the thick dashed line shows the ω^0 high-frequency decay.

become a useful tool to generate broadband seismograms for seismic hazard evaluation. At high frequencies, effects from small-scale velocity heterogeneities (Bydron & Dunham, 2015; Imperatori & Mai, 2012; Savran & Olsen, 2019; Withers et al., 2019,b), $Q(f)$, and nonlinear effects (Roten et al., 2017) become increasingly important. Armed with realistic broadband source descriptions from our KRG, it may be possible to resolve trade-offs between scattering parameters, nonlinearity, and $Q(f)$.

Mai et al. (2017) proposed a method to estimate λ using an anticorrelated random field with δ ; however, we could not reproduce their method using our dynamic rupture database. This is likely due to the sensitivity of λ to the orientation of the background stress field with respect to the fault plane in the dynamic rupture simulations. We recommend this question receive further scrutiny in the future.

Recently, Thingbaijam and Mai (2016) analyzed a database of finite-fault inversions and suggested that the slip distribution could be modeled using a truncated exponential distribution due to the positivity constraints on the physical rupture fields. In agreement with this study, we find that the mPDF estimates from our dynamic rupture models also follow truncated distributions. The truncated distributions provide representations of the rupture fields that are consistent with the physical limitations of the rupture process, namely, all rupture fields must be greater than zero. Figure 3a shows the marginal distributions estimated when considering all of the dynamic rupture simulations in our database. We find that the estimated density function is approximately symmetric, therefore we cannot account for the truncation at zero using a logarithmic transformation. In addition, we find that mPDFs are generally non-Gaussian, which is consistent with previous studies. Figure 3b shows quantile-quantile plots based on a standard normal variable. For

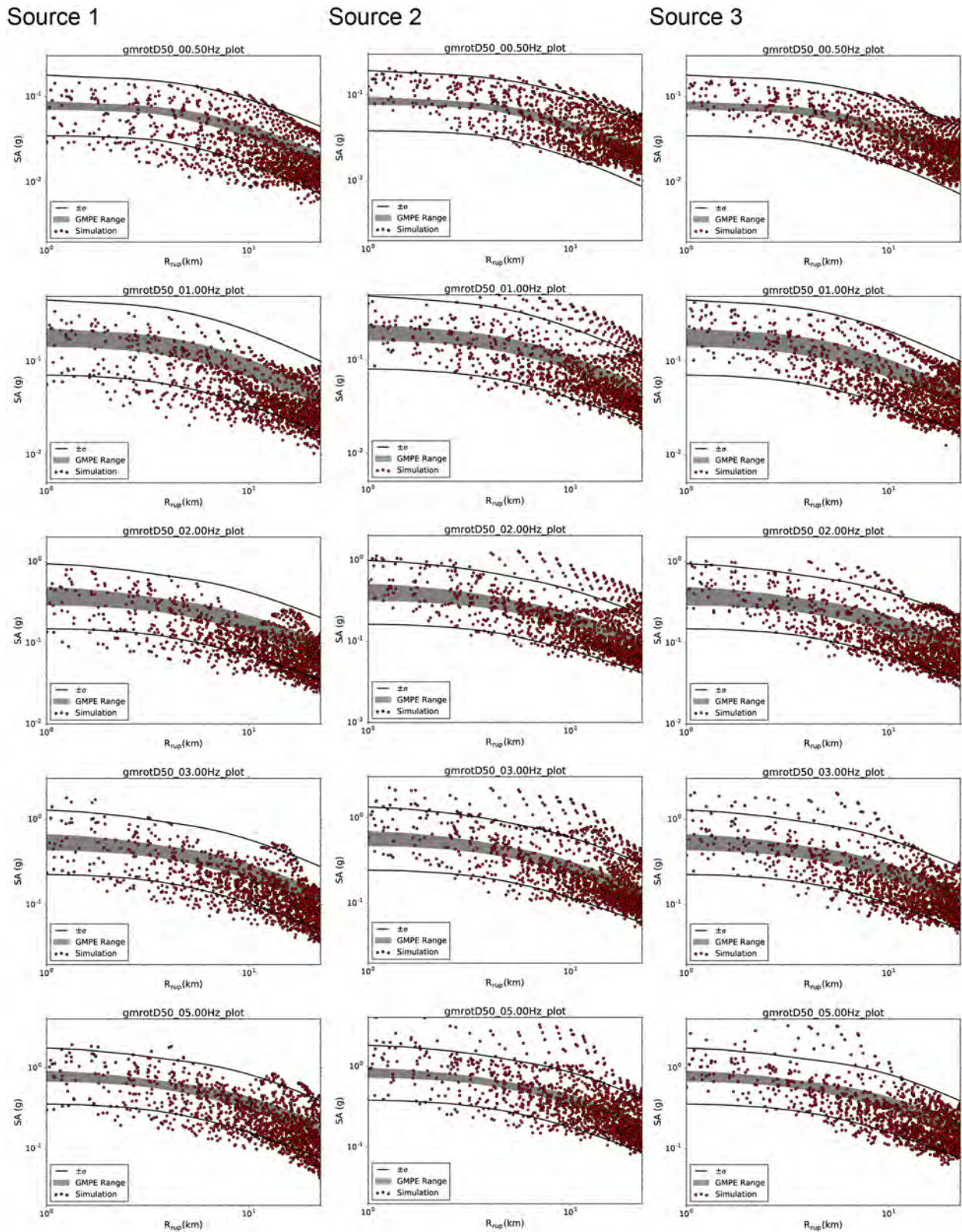


Figure 13. Comparisons of spectral accelerations for Source 1 (left), Source 2 (center), and Source 3 (right) against NGA West2 GMPE values. Red dots represent spectral acceleration values computed at the stations depicted (see Figure 5b). The shaded gray region shows the range of GMPE median estimates and the black line indicates ± 1 intraevent sigma.

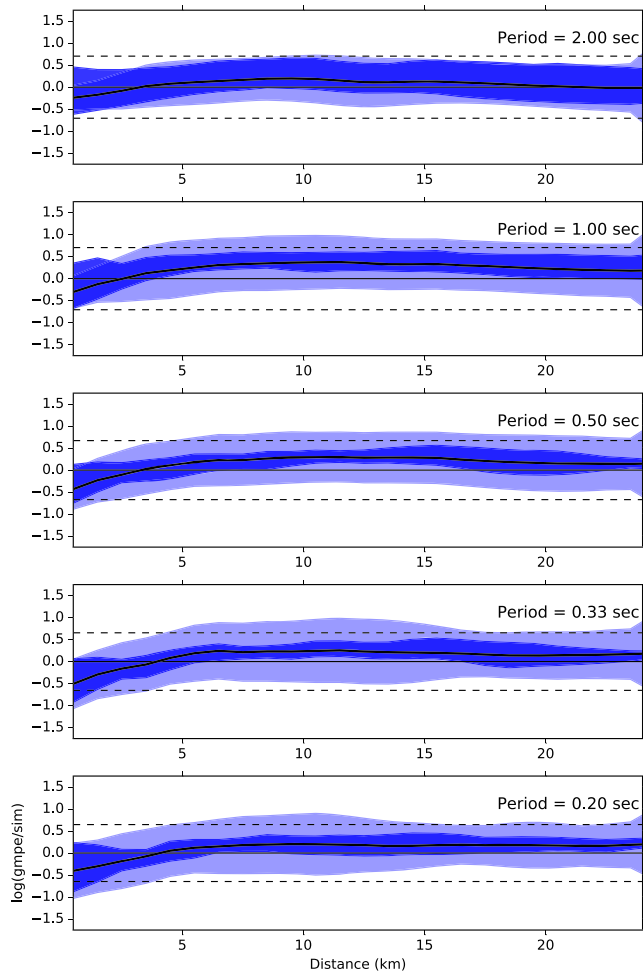


Figure 14. Bias plots comparing simulated median spectral accelerations for all five kinematic source models against GMPE medians. The thick black line depicts the ensemble average over all simulations, and the dark shaded blue region denotes the range of ensemble median values. The dashed black lines depict ± 1 intraevent σ (in natural log units) for each period predicted by the GMPE, and the light-shaded blue region shows the standard deviation in each distance bin from the simulated ensemble.

best represent the spatial statistics of observed slip models. In future work, we recommend to introduce more complex spatial correlation models that can account for some of the misfit observed in Figure 5. With our KRG implementation it is straightforward to incorporate more complex linear models of coregionalization or other covariance models.

Since we only simulated dynamic rupture models on strike-slip faults in a relatively limited magnitude range (M_w 6.5 to M_w 7.2), our rupture generator should only be used to simulate strike-slip sources in this magnitude range. Based on the fault dimensions in our rupture database there are data representing faults from 10 km \times 10 km up to 65 km \times 15 km. Previous studies have shown that dipping faults behave like strike-slip faults (Schmedes et al., 2013), in a statistical sense, but we recommend to confirm that relationship on rough faults before applying this model in that context. Lastly, scaling relationships should be adopted to expand this framework to various fault lengths.

7. Conclusions

This work is guided by the fact that a large part of the built infrastructure in our society consists of buildings that are particularly sensitive to ground motions with energy at frequencies between 1 and 10 Hz. For this

both Δu and V_{peak} the truncated values are observed at ~ -2.5 quantiles from the mean value. In our KRG, we incorporate an empirical mPDF derived from the dynamic rupture simulations, as opposed to using a general distribution function. Incorporating this type of generalized marginal distribution would be a primary target for future improvements to the KRG.

The implementation of this rupture generator is modular and flexible in the sense that nearly every aspect of the method can be easily improved or modified when new information becomes available. For instance, our choice to separate the physical source fields from estimating kinematic parameters allows for a straightforward incorporation of alternative source-time functions. In addition, the marginal distributions or two-point statistics could also be modified to reflect future analyses. Even the simulation technique itself could be replaced. This allows for a rupture generator that can evolve along with new information and understanding of the rupture process.

Despite promising comparisons with GMPEs, there are some limitations of this KRG from a practical standpoint. The most urgently needed improvement of the KRG is the ability to generalize the empirical cumulative distribution function for the simulated Δu and/or desired seismic moment. In the KRG's current form, the target M_w can only be chosen through specifying the fault dimension, as the empirical distribution functions for Δu , V_{peak} , and v_{rup}/c_s are fixed. In practice, as displayed by the five simulations shown in this article, the target M_w will vary depending on the result of the sequential simulation. This is caused by the fact that the sequential simulation method does not guarantee that the fields of a single realization will have zero mean, even though the random variable itself has zero mean. In future work, scaling relationships derived from the dynamic simulations supplemented with inverted kinematic sources, for example, following the approach of Melgar and Hayes (2019), can provide a framework that can generalize the rupture generator to sources not included in the dynamic rupture set used in our analysis.

Previous rupture generators implement power law or von Karman correlation functions to describe the autocorrelation structure. For example, Mai and Beroza (2002) find that von Karman autocorrelation functions

reason, it is critical to be able to predict shaking from future earthquakes in this bandwidth. Earthquake source characterization for the higher frequencies clearly requires further attention.

We have developed a new KRG based on the statistics of over 100 dynamic simulations on geometrically complex strike-slip faults for M 6.4–7.2 events to produce broadband ground motions. The KRG fits a linear model of coregionalization to capture the dominating behavior of the relevant scale lengths at the breakdown zone and along the slip path, respectively. In addition, we define empirical functions relating standard normal quantiles to the one-point statistics seen in the dynamic rupture simulations. We use a sequential technique to simulate realizations of this 4-D random variable conditioned on a distribution of the initial friction. Further validation and parameter tuning is needed to ensure that the KRG produces acceptable results for dip-slip events and magnitudes outside the range tested in this study.

We computed deterministic ground motion simulations for frequencies up to 10 Hz using five source models generated using the KRG implementation presented in this paper. We validate our ground motions for spectral accelerations with periods longer than 0.2 s against NGA West 2 GMPEs up to distances of 25 km. We find that our KRG produces ground motions that show promising comparisons with GMPE medians and intraevent standard deviations. In addition, our rupture generator produces flat acceleration across the desired model bandwidth as well as seismograms that qualitatively appear similar to recorded ground motions. Based on these comparisons, we believe that our rupture generator will help provide insight into the broadband behavior of future earthquakes. Future validation using this KRG should incorporate small-scale media heterogeneities and nonlinear response in the material surrounding the fault in order to capture other physical mechanisms involved in the wave propagation problem, and assess the interdependency between these parameters and the resulting ground motions. We propose these interdependencies could be investigated in a fully deterministic version of the SCEC broadband platform (Goulet et al., 2015). While this platform does not yet exist, it could be important for the future of high-frequency broadband ground motion simulation.

Data Availability Statement

The KRG software and data can be downloaded from this site (http://hypocenter.usc.edu/research/savran_olsen_krg).

Acknowledgments

We would like to thank Kyle Withers and an anonymous reviewer for their feedback that greatly improved this manuscript. We would also like to thank the editors for their thoughtful comments on the manuscript. This research was supported by NSF Awards OCI-1148493 (SI2-SSI) and EAR-1226343 EAR-1349180, and the Southern California Earthquake Center (SCEC). SCEC is funded by NSF Cooperative Agreement EAR-1033462 and USGS Cooperative Agreement G12AC20038. This is SCEC contribution 10083.

References

- Abrahamson, N. A., Silva, W. J., & Kamai, R. (2014). Summary of the ASK14 ground motion relation for active crustal regions. *Earthquake Spectra*, 30(3), 1025–1055. <https://doi.org/10.1193/070913EQS198M>
- Anderson, J. G., & Hough, S. (1984). A model for the shape of the Fourier amplitude spectrum of acceleration at high frequencies. *Bulletin of the Seismological Society of America*, 74(5), 1969–1993.
- Andrews, D. J. (1980). A stochastic fault model I. Static case. *Journal of Geophysical Research*, 85(NB7), 3867–3877. <https://doi.org/10.1029/jb085ib07p03867>
- Boore, D. M. (2006). Orientation-independent measures of ground motion. *Bulletin of the Seismological Society of America*, 96(4A), 1502–1511. <https://doi.org/10.1785/0120050209>
- Boore, D. M., Stewart, J. P., Seyhan, E., & Atkinson, G. M. (2014). NGA-West2 equations for predicting PGA, PGV, and 5% damped PSA for shallow crustal earthquakes. *Earthquake Spectra*, 30, 1057–1085.
- Brown, L., Wang, K., & Sun, T. (2015). Static stress drop in the M_w 9 Tohoku-oki earthquake: Heterogeneous distribution and low average value. *Geophysical Research Letters*, 42, 10,595–10,600. <https://doi.org/10.1002/2015GL066361>
- Bruno, J. N. (1970). Tectonic stress and the spectra of seismic shear waves from earthquakes. *Journal of Geophysical Research*, 75(26), 4997–5009. <https://doi.org/10.1029/JB075i026p04997>
- Bydlon, S. A., & Dunham, E. M. (2015). Rupture dynamics and ground motions from earthquakes in 2-D heterogeneous media. *Geophysical Research Letters*, 42, 1701–1709. <https://doi.org/10.1002/2014GL062982>
- Campbell, K. W., & Bozorgnia, Y. (2014). NGA-West2 ground motion model for the average horizontal components of PGA, PGV, and 5% damped linear acceleration response spectra. *Earthquake Spectra*, 30, 1087–1115. <https://doi.org/10.1193/062913EQS175M>
- Candela, T., Renard, F., Klinger, Y., Mair, K., Schmittbuhl, J., & Brodsky, E. E. (2012). Roughness of fault surfaces over nine decades of length scales. *Journal of Geophysical Research*, 117, B08409. <https://doi.org/10.1029/2011JB009041>
- Chiou, B. S. J., & Youngs, R. R. (2014). Update of the Chiou and Youngs NGA model for the average horizontal component of peak ground motion and response spectra. *Earthquake Spectra*, 30(3), 1117–1153. <https://doi.org/10.1193/072813EQS219M>
- Cui, Y., Olsen, K. B., Jordan, T. H., Lee, K., Zhou, J., Small, P., et al. (2010). Scalable earthquake simulation on petascale supercomputers. *International Conference for High Performance Computing, Networking, Storage and Analysis*, 1–20. <https://doi.org/10.1109/SC.2010.45>
- Cui, Y., Poyraz, E., Olsen, K. B., Zhou, J., Withers, K. B., Callaghan, S., et al. (2013). Physics-based seismic hazard analysis on petascale heterogeneous supercomputers. *Proceedings of the International Conference on High Performance Computing, Networking, Storage and Analysis*, 70. <https://doi.org/10.1145/2503210.2503300>

- Dalguer, L. A., Miyake, H., Day, S. M., & Irikura, K. (2008). Surface rupturing and buried dynamic-rupture models calibrated with statistical observations of past earthquakes. *Bulletin of the Seismological Society of America*, *98*(3), 1147–1161. <https://doi.org/10.1785/0120070134>
- Dunham, E. M., Belanger, D., Cong, L., & Kozdon, J. E. (2011). Earthquake ruptures with strongly rate-weakening friction and off-fault plasticity, Part 2: Nonplanar faults. *Bulletin of the Seismological Society of America*, *101*(5), 2308–2322. <https://doi.org/10.1785/0120100076>
- Ely, G. P., Day, S. M., & Minster, J.-B. (2008). A support-operator method for viscoelastic wave modelling in 3-D heterogeneous media. *Geophysical Journal International*, *172*(1), 331–344. <https://doi.org/10.1111/j.1365-246X.2007.03633.x>
- Ely, G. P., Day, S. M., & Minster, J.-B. (2009). A support-operator method for 3-D rupture dynamics. *Geophysical Journal International*, *177*(3), 1140–1150. <https://doi.org/10.1111/j.1365-246X.2009.04117.x>
- Fang, Z., & Dunham, E. M. (2013). Additional shear resistance from fault roughness and stress levels on geometrically complex faults. *Journal of Geophysical Research: Solid Earth*, *118*, 3642–3654. <https://doi.org/10.1002/jgrb.50262>
- Goovaerts, P., & Goovaerts, P. (1997). *Geostatistics for natural resources evaluation*. New York, New York: Oxford University Press.
- Goulet, C. A., Abrahamson, N. A., Somerville, P. G., & Wooddell, K. E. (2015). The SCEC broadband platform validation exercise for pseudo-spectral acceleration: Methodology for code validation in the context of seismic hazard analyses. *Seismological Research Letters*, *86*(1), 17–26. <https://doi.org/10.1785/0220140104>
- Graves, R. W., Jordan, T. H., Callaghan, S., Deelman, E., Field, E. H., Juve, G., et al. (2011). CyberShake: A physics-based seismic hazard model for Southern California. *Pure and Applied Geophysics*, *168*(3–4), 367–381. <https://doi.org/10.1007/s00024-010-0161-6>
- Graves, R. W., & Pitarka, A. (2014). Refinements to the Graves and Pitarka (2010) broadband ground-motion simulation method. *Seismological Research Letters*, *86*(1), 75–80. <https://doi.org/10.1785/0220140101>
- Graves, R. W., & Pitarka, A. (2016). Kinematic ground motion simulations on rough faults including effects of 3D stochastic velocity perturbations. *Bulletin of the Seismological Society of America*, *106*(5), 2136–2153. <https://doi.org/10.1785/0120160088>
- Gutteri, M., Mai, P. M., & Beroza, G. C. (2004). A pseudo-dynamic approximation to dynamic rupture models for strong ground motion prediction. *Bulletin of the Seismological Society of America*, *94*(6), 2051–2063. <https://doi.org/10.1785/0120040037>
- Hanks, T. C., & Bakun, W. H. (2014). M-log A models and other curiosities. *Bulletin of the Seismological Society of America*, *104*(5), 2604–2610.
- Harris, R. A., Barall, M., Archuleta, R., Dunham, E. M., Aagaard, B. T., Ampuero, J. P., et al. (2009). The SCEC/USGS dynamic earthquake rupture code verification exercise. *Seismological Research Letters*, *80*(1), 119–126. <https://doi.org/10.1785/gssrl.80.1.119>
- Imperatori, W., & Mai, P. M. (2012). Broad-band near-field ground motion simulations in 3-dimensional scattering media. *Geophysical Journal International*, *192*(2), 725–744. <https://doi.org/10.1093/gji/ggs041>
- Leonard, M. (2010). Earthquake fault scaling: Self-consistent relating of rupture length, width, average displacement, and moment release. *Bulletin of the Seismological Society of America*, *100*(5A), 1971–1988. <https://doi.org/10.1785/0120090189>
- Ma, S., & Andrews, D. J. (2010). Inelastic off-fault response and three-dimensional dynamics of earthquake rupture on a strike-slip fault. *Journal of Geophysical Research*, *115*, B04304. <https://doi.org/10.1029/2009JB006382>
- Mai, P. M., & Beroza, G. C. (2002). A spatial random field model to characterize complexity in earthquake slip. *Journal of Geophysical Research*, *107*(B11), 2308. <https://doi.org/10.1029/2001JB000588>
- Mai, P. M., Galis, M., Thingbaijam, K. K. S., Vyas, J. C., & Dunham, E. M. (2017). Accounting for fault roughness in pseudo-dynamic ground-motion simulations. *Pure and Applied Geophysics PAGEOPH*, *174*(9), 3419–3450. <https://doi.org/10.1007/s00024-017-1536-8>
- Marcinkovich, C., & Olsen, K. B. (2003). On the implementation of perfectly matched layers in a three-dimensional fourth-order velocity-stress finite difference scheme. *Journal of Geophysical Research*, *108*(B5), 2276. <https://doi.org/10.1029/2002JB002235>
- Melgar, D., & Hayes, G. P. (2019). The correlation lengths and hypocentral positions of great earthquakes. *Bulletin of the Seismological Society of America*, *109*(6), 2582–2593. <https://doi.org/10.1785/0120190164>
- Ohnaka, M., & Yamashita, T. (1989). A cohesive zone model for dynamic shear faulting based on experimentally inferred constitutive relation and strong motion source parameters. *Journal of Geophysical Research*, *94*(B4), 4089–4104. <https://doi.org/10.1029/JB094iB04p04089>
- Olsen, K. B., Day, S. M., Dalguer, L. A., Mayhew, J., Cui, Y., Zhu, J., et al. (2009). ShakeOut-D: Ground motion estimates using an ensemble of large earthquakes on the southern San Andreas fault with spontaneous rupture propagation. *Geophysical Research Letters*, *36*, L04303. <https://doi.org/10.1029/2008GL036832>
- Olsen, K. B., & Takedatsu, R. (2015). The SDSU broadband ground-motion generation module BBtoolbox version 1.5. *Seismological Research Letters*, *86*(1), 81–88. <https://doi.org/10.1785/0220140102>
- Oreskes, N., Shraderfrechette, K., & Belitz, K. (1994). Verification, validation, and confirmation of numerical-models in the earth-sciences. *Science*, *263*(5147), 641–646. <https://doi.org/10.1126/science.263.5147.641>
- Pitarka, A., Dalguer, L. A., Day, S. M., Somerville, P. G., & Dan, K. (2009). Numerical study of ground-motion differences between buried-rupturing and surface-rupturing earthquakes. *Bulletin of the Seismological Society of America*, *99*(3), 1521–1537. <https://doi.org/10.1785/0120080193>
- Roten, D., Olsen, K. B., & Day, S. M. (2017). Off-fault deformations and shallow slip deficit from dynamic rupture simulations with fault zone plasticity. *Geophysical Research Letters*, *44*, 7733–7742. <https://doi.org/10.1002/2017GL074323>
- Roten, D., Olsen, K. B., Day, S. M., Cui, Y., & Faeh, D. (2014). Expected seismic shaking in Los Angeles reduced by San Andreas fault zone plasticity. *Geophysical Research Letters*, *41*, 2769–2777. <https://doi.org/10.1002/2014GL059411>
- Savran, W. H., & Olsen, K. B. (2019). Ground motion simulation and validation of the 2008 Chino Hills earthquake in scattering media. *Geophysical Journal International*, *219*(3), 1836–1850. <https://doi.org/10.1093/gji/ggz399>
- Schmedes, J., Archuleta, R. J., & Lavalley, D. (2010). Correlation of earthquake source parameters inferred from dynamic rupture simulations. *Journal of Geophysical Research*, *115*, B03304. <https://doi.org/10.1029/2009JB006689>
- Schmedes, J., Archuleta, R. J., & Lavalley, D. (2013). A kinematic rupture model generator incorporating spatial interdependency of earthquake source parameters. *Geophysical Journal International*, *192*(3), 1116–1131. <https://doi.org/10.1093/gji/ggs021>
- Shearer, P. M., Prieto, G. A., & Hauksson, E. (2006). Comprehensive analysis of earthquake source spectra in southern California. *Journal of Geophysical Research*, *111*, B06303. <https://doi.org/10.1029/2005JB003979>
- Shi, Z., & Day, S. M. (2013). Rupture dynamics and ground motion from 3-D rough-fault simulations. *Journal of Geophysical Research - Solid Earth*, *118*, 1122–1141. <https://doi.org/10.1002/jgrb.50094>
- Song, S. G. (2015). Developing a generalized pseudo-dynamic source model of $M_w6.5-7.0$ to simulate strong ground motions. *Geophysical Journal International*, *204*(2), 1254–1265. <https://doi.org/10.1093/gji/ggv521>

- Song, S. G., Dalguer, L. A., & Mai, P. M. (2013). Pseudo-dynamic source modelling with 1-point and 2-point statistics of earthquake source parameters. *Geophysical Journal International*, *196*(3). <https://doi.org/10.1093/gji/ggt479>
- Thingbaijam, K. K. S., & Mai, P. M. (2016). Evidence for truncated exponential probability distribution of earthquake slip. *Bulletin of the Seismological Society of America*, *106*(4), 1802–1816. <https://doi.org/10.1785/0120150291>
- Tinti, E., Cocco, M., Fukuyama, E., & Piatanesi, A. (2009). Dependence of slip weakening distance (D_c) on final slip during dynamic rupture of earthquakes. *Geophysical Journal International*, *177*(3), 1205–1220. <https://doi.org/10.1111/j.1365-246X.2009.04143.x>
- Tinti, E., Fukuyama, E., & Piatanesi, A. (2005). A kinematic source-time function compatible with earthquake dynamics. *Seismological Society of America*, *95*(4), 1211–1223. <https://doi.org/10.1785/0120040177>
- Trugman, D. T., & Dunham, E. M. (2014). A 2D pseudodynamic rupture model generator for earthquakes on geometrically complex faults. *Bulletin of the Seismological Society of America*, *104*(1), 95–112. <https://doi.org/10.1785/0120130138>
- Wells, D. L., & Coppersmith, K. J. (1994). New empirical relationships among magnitude, rupture length, rupture width, rupture area, and surface displacement. *Bulletin of the Seismological Society of America*, *84*(4), 974–1002.
- Withers, K. B., Olsen, K. B., & Day, S. M. (2015). Memory-efficient simulation of frequency-dependent Q . *Bulletin of the Seismological Society of America*, *105*(6), 3129–3142. <https://doi.org/10.1785/0120150020>
- Withers, K. B., Olsen, K. B., Day, S. M., & Shi, Z. (2019). Ground motion and intraevent variability from 3D deterministic broadband (0–7.5 Hz) simulations along a nonplanar strike-slip fault. *Bulletin of the Seismological Society of America*, *109*(1), 229–250. <https://doi.org/10.1785/0120180006>
- Withers, K. B., Olsen, K. B., Shi, Z., & Day, S. M. (2019). Validation of deterministic broadband ground motion and variability from dynamic rupture simulations of buried thrust earthquakes validation of deterministic broadband ground motion and variability. *Bulletin of the Seismological Society of America*, *109*(1), 212–228. <https://doi.org/10.1785/0120180005>
- Xu, X., Tong, X., Sandwell, D. T., Milliner, C. W. D., Dolan, J. F., Hollingsworth, J., et al. (2016). Refining the shallow slip deficit. *Geophysical Journal International*, *204*(3), 1843–1862. <https://doi.org/10.1093/gji/ggv563>
- Yao, Q. (2017). Dynamic Modeling of earthquake sources on rough faults. Dissertation UC San Diego. Retrieved from (<http://escholarship.org/content/qt3h37c2x5/qt3h37c2x5.pdf>).
- Yoffe, E. H. (1951). The moving Griffith crack. *The London, Edinburgh, and Dublin Philosophical Magazine and Journal of Science*, *42*(330), 739–750. <https://doi.org/10.1080/14786445108561302>
- Zoback, M. D., Zoback, M. L., Mount, V. S., Suppe, J., Eaton, J. P., Healy, J. H., et al. (1987). New evidence on the state of stress of the San Andreas Fault System. *Science*, *238*(4830), 1105–1111. <https://doi.org/10.1126/science.238.4830.1105>

References From the Supporting Information

- Christakos, G. (1984). On the problem of permissible covariance and variogram models. *Water Resources Research*, *20*(2), 251–265. <https://doi.org/10.1029/WR020i002p00251>